

Article

DEM Based Study on Shielded Astronomical Solar Radiation and Possible Sunshine Duration under Terrain Influences on Mars by Using Spectral Methods

Siwei Lin and Nan Chen *

The Academy of Digital China (Fujian), Fuzhou University, Fuzhou 350108, China; n195520011@fzu.edu.cn

* Correspondence: chennan@fzu.edu.cn

Abstract: Solar radiation may be shielded by the terrain relief before reaching the Martian surface, especially over some rugged terrains. Yet, to date, no comprehensive studies on the spatial structure of shielded astronomical solar radiation (SASR) and the possible sunshine duration (PSD) on Mars have been conducted by previous researchers. Previous studies generally ignored the influences of the terrain on the SASR and PSD, which resulted in a corresponding unexplored field on SASR. The purpose of this paper is to study the Martian spatial-temporal structure of SASR and the PSD under terrain influences. In this paper, the theory of Earth's SASR, the previous Martian SASR model and the theory of planetary science were combined to propose the SASR model that can be applied to Mars. Then, with the spectrum method theory of geography, we defined two new concepts of spectrums to explore the spatial-temporal distribution of SASR and PSD in different Martian landforms. We found SASR and PSD on Mars were significantly influenced by terrain relief and latitude and showed sufficient regularity, which can be concluded as a gradual attenuation with terrain relief and a regularity of latitude anisotropy. The latitude anisotropy feature is a manifestation of the terrain shielding effect. With the latitude varying, SASR and PSD at different temporal scale generally showed different features with those of Earth, which may be attributed to the imbalanced seasons caused by Martian moving orbits and velocity. Compared to PSD, SASR showed more regular variation under terrain relief and was more influenced by the terrain relief which revealed that SASR is more sensitive to terrain relief than PSD. Additionally, the critical area is a quantitative index to reflect the stable spatial structure of SASR and PSD in different landforms and may be viewed as the minimum test region of sample areas. The corresponding result of the experiments herein indicated that either spectrum can effectively depict the spatial-temporal distribution of SASR and PSD on Mars under terrain relief and deepen the understanding of the variation of SASR and PSD influences by terrain. The critical area of either spectrum can be employed to explore and determine the stable spatial structure of SASR and PSD in different landforms. The proposed Martian SASR model and the new spectral method theory shed new light on revealing the spatial-temporal structure of SASR and PSD under terrain influences on Mars.

Keywords: DEM; terrain relief; spectrum; roughness; shielding effect; shielded astronomical solar radiation; possible sunshine duration



Citation: Lin, S.; Chen, N. DEM Based Study on Shielded Astronomical Solar Radiation and Possible Sunshine Duration under Terrain Influences on Mars by Using Spectral Methods. *ISPRS Int. J. Geo-Inf.* **2021**, *10*, 56. <https://doi.org/10.3390/ijgi10020056>

Academic Editors: Wolfgang Kainz and Josef Stöbl

Received: 11 December 2020

Accepted: 27 January 2021

Published: 30 January 2021

Publisher's Note: MDPI stays neutral with regard to jurisdictional claims in published maps and institutional affiliations.



Copyright: © 2021 by the authors. Licensee MDPI, Basel, Switzerland. This article is an open access article distributed under the terms and conditions of the Creative Commons Attribution (CC BY) license (<https://creativecommons.org/licenses/by/4.0/>).

1. Introduction

Solar radiation, as an important power source, plays a vital role in agricultural production and applications of photovoltaic power generation systems on Mars [1]. photovoltaic power systems, possessing many advantages, including high power-to-weight ratio, high efficiency, modularity, scalability, and a long history of successful application in space, are required on the mission to the Martian surface [2]. Detail information on the characteristics of solar radiation on Mars is necessary for the effective design of future planned photovoltaic systems operating on the surface of Mars [3]. The exploration of the spatial-temporal distribution of solar radiation on Mars will help to deepen our understanding of

the Martian radiation environment [4]. Besides, solar radiation is a fundamental energy of agriculture production. Agriculture production is crucial to the process of building a habitable environment on Mars, thereby leading to an ever-increasing demand for solar radiation [5]. The issue of the Martian solar radiation calculation, thus, is of increasing importance and has received much attention.

The solar radiation reaching the surface of the planet without the consideration of atmospheric effects is named extraterrestrial solar radiation (ESR) [6–11]. Additionally, since it may be shielded by the terrain relief when it reaches a rugged surface, it is also named shielded astronomical solar radiation (SASR) [11,12]. SASR, representing the foundational data and the determining component of solar radiation [11], is a fundamental factor to estimate solar energy resource [6,13] and a model to simulate crop photosynthesis and transpiration [14–16]. It has a major impact on hydrological and biological applications and climate monitoring. Based on atmosphere parameters, it was used to calculate direct radiation, diffuse reflection, and total radiation. i.e., the construction of the SASR model is the basis of solar radiation. Previous research works revealed that the quantity of the SASR (or solar radiation) on the surface has strong connections to the terrain influences: slope and aspect, and the terrain shielding effect [6,7,12,16–19]. The sunshine duration (SD) that determines the amount of solar radiation and solar energy is a critical calculation variable in SASR calculation [20,21]. The possible sunshine duration (PSD) refers to the sunshine duration which takes account of the terrain influences in this paper. The PSD structure also shows an intimate relationship to terrain influences: slope, aspect, and terrain relief effect [14,22–24].

Numerous models to calculate solar radiation on Mars, which can be divided into the solar radiation on the Martian surface [1–3,9,10,25–39] and the solar radiation on the Martian atmosphere [2,4,9,29,30,38–54], are now available. Furthermore, solar radiation on the Martian surface can be divided into the SASR, direct solar radiation, diffuse solar radiation, and total solar radiation. The intensity of solar radiation on Mars is mainly influenced by the following factors: (1) Mars–Sun distance; (2) astronomical and geographical factors (areocentric longitude, solar zenith angle, solar declination angle, etc.); (3) atmospheric physical factors (atmospheric transparency, optical depth, and opacity of the Martian atmosphere, etc.); (4) the position of the planet and corresponding Martian day; and (5) terrain influences (slope, aspect, terrain relief effect, etc.) [1,2,27]. Although research on the solar radiation model has been extensive, the current solar radiation models on Mars are restricted to be constructed based on the first four factors [1–4,26,27,29,38,41–45,51,54–56]. Namely, the fourth influencing factor, surrounding terrain influences, is generally ignored in this field. Although many researchers have explored the optimum slope and orientation of a surface receiving solar radiation on the Martian surface through various ways [1,27,32], they only considered the slope and orientation of solar energy collectors, which did not consider local terrain characteristics: slope, aspect, and the surrounding terrain.

The terrain influences exert great uncertainty on the calculation of SASR and solar radiation. The previous research works have proven that local terrain characteristics (aspect, slope) have a great effect on the quantities of solar radiation reaching the ground [6,14,16,23,57–63]. Furthermore, the solar radiation falling on rugged terrains is not only affected by terrain factors (aspect and slope), but also by surrounding terrain [11,12,58,59,63]. Namely, when solar radiation arrives at a given position on the Martian surface, it may be shielded by the terrain relief around the position if it is in a rugged area. The shielding effect caused by terrain relief leads to great uncertainty in the calculations of SASR [18,19,61,63–65]. Particularly, owing to the complex and diverse Martian landforms and the large structural differences of regional terrains, the shielding effect may lead to considerable influences on the spatial distribution of solar radiation for different landforms. The terrain influences are indispensable considerations in the spatial structure of the simulation on solar radiation. Consequently, these previous results were unsatisfactory as the uncertainties of terrain influences still exist. To summarize, the limitations of the previous research were that they were failed to take account of the

terrain influences around the given position on solar radiation. It is of great significance to consider the terrain influences of the solar radiation model and to study the effects of terrains on solar radiation.

Since the research about SASR and PSD on Mars does not take terrain influences into account, the research about SASR and PSD taking terrain influences into account is an unexplored field in the current study of solar radiation on Mars. A large number of papers have studied the SASR and PSD over rugged terrains for different sites on Earth [5,6,16,19,22,23,58,59,63,66–68]. On the contrary, little attention has been paid to Mars. Although in recent years the concept of SASR has been proposed on Mars, it is still in an embryonic form and the corresponding previous studies approximated astronomical radiation as the total solar radiation at the vertical surface or atmosphere, regardless of the topography [9,10,38,69–72]. It may mainly because the information lacking in the database restricts our research potential. However, the conditions are already in place for the calculations of SASR and PSD on Mars. Combining the existing planetary astronomy theory and Earth astronomy radiation model, we can simulate the Martian SASR and PSD. Meanwhile, the Mars Orbiter Laser Altimeter data (MOLA data) data, which was derived from the Mars Orbiter Laser Altimeter, is now available and enables the calculations of SASR and PSD. Given the above, it is significant to reconstruct SASR model (or PSD model) and study the terrain influences on SASR and PSD. The SASR and PSD models, which are closely related to the terrains, deserve more attention.

Roughness, the mathematical expression of surface relief in a specific area, reflects the extent of the surface relief. It can clearly distinguish different geomorphic units [73]. Roughness derived from statistical analysis of MOLA data may be a useful tool for interpreting the Martian surface properties and revealing the origin and evolution of geologic units [74]. “The variations in topographic parameters exert a strong influence on the amount of solar radiation received by two adjacent locations”, which has been found in [18]. As mentioned above, the SASR on the surface is related to the terrain relief. Besides, the spatial structures of the SASR and PSD are influenced by the slope. Also, there is a functional relationship between roughness and slope [75]. In summary, based on the above-mentioned findings, the roughness can be a parameter that reveals the extent of terrain influences on spatial structures of SASR.

Yet, to date, no comprehensive study for spatial-temporal distribution of SASR and PSD on Mars has been conducted. Research on the subject has received scant attention in the corresponding papers and has been mostly restricted to limited analysis. The study of the spatial-temporal distribution of solar radiation on Mars is at a relatively preliminary stage; besides, the existing research on the spatial-temporal distribution of solar radiation on Mars is mainly based on the relatively crude solar radiation model. Some studies revealed the effects of climatic conditions (carbon dioxide, magnetic field, dust, etc.) or atmospheric phenomenon on solar radiation by exploring the environmental variations and laws of the Martian atmosphere [4,38,39,41,42,44,46,49,51,54]; some researchers improved the original solar radiation model or constructed another solar radiation models according to atmospheric properties or atmospheric factors [43,45,50,51]; some researchers studied the solar radiation reaching the Martian surface by developed models that used updating radiative parameters, meteorological parameters or topographic parameters [1,10,26,29,30,32,37]. These works generally aimed to investigate the variation laws of solar radiation on Mars under the influence of the environment or improve the quantity and precision of the solar radiation, which resulted in a relatively limited study of the spatial-temporal distribution of solar radiation on Mars.

These results, using the comparative analysis and the statistical analysis, carried out a certain degree of analysis on solar radiation’s spatial distribution. However, these analyses invariably took one Martian solar day as the unit for research, which ignored the effect of the time angle on the Martian surface and may cause the time accuracy to be relatively limited. Additionally, as mentioned above, although the solar radiation model was improved and reconstructed in various ways, terrain factors and terrain shielding

effect was still out of consideration. As described, the effect of surrounding terrain may increase the huge uncertainty of solar radiation, especially on Mars, which is much more rugged than Earth. In other words, we may get an inaccurate spatial structure of solar radiation in mountains. Ultimately, due to the complex topology, the huge area, and the limitations of existing data, the existing previous research generally analyzed the solar radiation globally or at one certain site macroscopically and quantitatively, which failed to analyze the spatial distribution at a regional scale. Also, the current classification of the Martian topography is artificial. However, Mars has not been sufficiently explored. So far, only USGS and NASA have made simple and rough terrain classification, possibly resulting in an inaccurate terrain division. The specific landform has specific solar radiation characteristics, and the research on artificially defined sample area may be unable to accurately reveal the characteristics in the spatial-temporal distribution of solar radiation for the specific landform. These deficiencies lead to certain limitations of current research on SASR and PSD.

These limitations may lead us to obtain the inaccurate characteristics and spatial-temporal structure of SASR and PSD on Mars. Besides, we may get a wrong cognition of the spatial-temporal distribution variations of SASR and PSD which may be caused by the influence of the terrain. Moreover, since the terrain may influence the spatial structure of the solar energy received at the terrain surface, we may fail to be aware of how the terrain affects the received solar radiation for solar energy collectors on Mission to Mars. Given the above, under the premise of constructing the SASR and PSD model, it is of the utmost importance to find an effective method which is cable to study the SASR's spatial and temporal distribution under terrain influences as well as the influences of terrain relief effect on SASR's distributions for different Martian landforms. To this end, this research seeks to overcome these limitations.

The spectrum method, which has not been used in the study of Mars, is an effective method to reflect the spatial and temporal distribution of phenomena according to the law of gradual varies or distribution of certain indexes. It has been developed to successfully reveal the spatial structure of the slope, i.e., the slope spectrum [76–80]. Moreover, it was first successfully employed in SASR and PSD on Earth to reveal the spatial structure of SASR and PSD based on slope spectrum [11,12]. It is an organic combination and bold attempt of Earth science and astronomy theory. Since the Martian geomorphology meets the statistical fractal characteristic, namely, the self-similarity characteristics of the regional geomorphology required by the spectral method [79,81], the spectral method can be applied to Martian research.

The spectrum method, as an effective method, can depict the spatial structure more accurately and comprehensively than other methods [11,12,77–79]. Moreover, the determination of critical areas in deriving spectra is an indispensable task [78,79]. When it is employed to analyze the SASR and PSD, it can accurately extract the stable area of SASR and PSD for different specific geomorphology [11,12], to avoid making wrong judgments on solar radiation characteristics. In other words, it is efficient in determining the stable spatial area for SASR and PSD of different Martian landforms, which may help us avoid the uncertainty caused by artificial division. Specifically, it can intuitively present the spatial distribution of SASR under different topographic relief in the form of a two-dimensional spectrum, which is convenient for us to analyze the degree of the SASR and PSD affected by topography and explore the spatio-temporal variation rules of SASR affected by topography. It is an effective method that can accurately and comprehensively reveal the distribution of SASR and PSD in specific landform and quantify the SASR and PSD under different topographic relief.

By constructing a two-dimensional spectrum of SASR and topographic relief factor, the extent of SASR affected by topographic relief can be effectively evaluated. By constructing the SASR spectrum at different temporal scales (season, month, and year), we can deepen our understanding of the variations and differences for geomorphic shielding effect of solar radiation at different durations. These advantages suggest that it can deal with most

of the current existing bottlenecks mentioned above. Therefore, the spectral method is undoubtedly a valuable method for the special research status of Mars.

The specific objective of this study is to explore the spatial distribution of SASR and PSD and reveal the spatial relationship between SASR and surrounding terrain effects. The innovation points of the research can be divided into the following aspects: (1) Based on the Martian solar radiation theory, combined with Earth's SASR theory and astronomical theories, we offer the theories of SASR which have not been used on the Martian surface. This theory takes the terrain influences into account. Also, the unit for calculating the SASR is improved from one sol to twenty minutes. It somewhat enhances the shortcomings of the current Martian solar radiation model and can be employed as the basis for future Martian solar radiation calculations. (2) According to the particular topography and the limited data sources of Mars, to investigate the spatial-temporal distribution of SASR at a regional scale for different Martian landforms, one concept of spectrum method is proposed in this paper. It is an effective framework in which researchers can explore the spatial-temporal structure of SASR and PSD influenced by topography. The theory of this paper can provide a reference for the analysis on the spatial structure of other meteorological factors. Furthermore, by extracting the stable areas for different landforms, it is an efficient method that can accurately and comprehensively reveal the SASR's distribution of specific landforms regionally and quantify the solar radiation under different topographic relief. It can be concluded that the aim of this paper is to fill the gap in the studies on the analysis of spatial-temporal law of SASR on Mars, enrich and improve the theories and methods of solar radiation on the Martian surface.

2. Materials and Methods

2.1. Materials

The representative landforms on the Martian surface are volcanoes, impact craters, Vallis, mountain range, planitia, plateau, dune fields, and Colinas [82,83]. The analysis and interpretation of Martian geomorphologic features are mainly focused on the above mentioned typical geomorphologies [84–89]. Note that dunes are too flat to be extracted by spectral method (it may be lack of topographic feature information), thus this paper focused on the other seven landforms (further discussion see Section 4.3). All other typical landforms of Mars mentioned above which have been deeply investigated by previous researchers have been used in this paper as sample areas (see Table 1).

Table 1. Introduction to the four sample areas.

| Sample Areas | Center Longitude | Center Latitude | Landform |
|--------------------|------------------|-----------------|----------------|
| Galaxias Colles | 347.78° | 39.07° | Colina |
| Kasei Valles | 297.12° | 25.14° | Vallis |
| Arena Colles | 82.93° | 24.63° | Colina |
| Olympus Mons | 226.2° | 18.65° | Volcanoes |
| Amenthes Plalatumn | 105.92° | 3.4° | Plateau |
| Libya Montes | 88.23° | 1.44° | mountain range |
| schiaparelli | 16.77° | −2.71° | impact craters |
| Arsia Mons | 239.91° | −8.26° | volcanoes |
| Huygen | 55.58° | −13.88° | impact craters |
| Valles Marineris | 301.41° | −14.01° | vallis |
| Eridania Planitia | 122.21° | −38.15° | planitia |
| Charitum Montes | 319.71° | −58.1° | mountain range |

Note that in order to confirm and demonstrate some conclusions for this paper and analyze the degree of SASR and PSD affected by shielding effect in different geographical locations, the latitude of sampling area ranges from north latitude 39.07° to south latitude 58.1° (see Table 1). The spectral method was successfully used in these sample areas and the stable area was extracted successfully.

The data to calculate SASR and PSD is the Mars MGS MOLA - MEX HRSC Blended DEM. It is a blend of digital elevation model (DEM) data derived from the Mars Orbiter Laser Altimeter (MOLA) and the High-Resolution Stereo Camera (HRSC). It is the latest data improved from MOLA data. Its resolution accuracy is 200 m, which is significantly improved compared to the original MOLA data. It is published by USGS Astrogeology Science Center and can be downloaded from the website: https://astrogeology.usgs.gov/search/map/Mars/Topography/HRSC_MOLA_Blend/Mars_HRSC_MOLA_BlendDEM_Global_200mp_v2. All the SASR and PSD of different landforms can be calculated from the MOLA data of the corresponding sample areas.

2.2. Method to Compute the PSD and SASR

2.2.1. The Law of Revolution and Rotation of Mars

Mars is a planet. In common with the Earth, Mars moves around the sun. Besides, according to Kepler's laws, it moves around sun in an elliptical orbit like the Earth. The average distance between Mars and the sun is 1.52 astronomical unit (AU). Its orbital period is 669 solar day (687 Earth days) [90]. In common with the Earth, Mars rotates constantly. A solar day(sol) on Mars, which is its rotation cycle and only slightly longer than an Earth day, is 24.6230556 h [91]. Martian eccentricity is 0.093377. Martian obliquity of rotation axis is 25.19° [92,93]. According to the law of revolution and rotation of Mars, we can calculate the astronomical solar radiation at the top of the Martian atmosphere. Then, we can obtain the Equations of the astronomical solar radiation on the slope surface. Based on the calculation model of SASR on the sloped surface, we can reconsider the corresponding Equations and build the distributed model (or subparagraph integral mathematical model) to calculate PSD and SASR under terrain relief on Mars. Based on the existing theoretical model of solar radiation on Mars [1,2,9,10,26,27,30,32,37–39] and the Astronomical theory on Mars, combining with the theoretical model of solar radiation on Earth [6,8,11,12,14,15,17,63,64,91,94–101], the SASR model which is suitable for Mars is proposed. It can be given by the following steps:

2.2.2. Calculation Model of the PSD and SASR on the Sloped Surface

The SASR at the top of the atmosphere can be calculated by the following equation [2,6,27,96]:

$$Q_1 = \left(\frac{1}{\rho}\right)^2 I_0, \quad (1)$$

where Q_1 is the SASR at the top of the Martian atmosphere, $\left(\frac{1}{\rho}\right)$ is the calibration coefficient of solar-Mars distance, I_0 is the solar constant of Mars. The SASR irradiance on the sloped surface can be calculated by the following equation:

$$Q_0 = Q_1 \cos \theta_1 = \left(\frac{1}{\rho}\right)^2 I_0 \cos \theta_1, \quad (2)$$

where θ_1 is the solar illumination angle(or solar incident angle) on the sloped surface. $\cos \theta_1$, which is the reduced form of Equation (14) in [1] or Equation (2.10) in paper [27], can be calculated by the following equation [1,27,63,94,96,102]:

$$\cos \theta_1 = U \sin \delta + V \cos \delta \cos \omega + W \cos \delta \sin \omega, \quad (3)$$

Thus, the SASR irradiance on the sloped surface can be calculated by the following equation [6,14]:

$$Q_0 = \left(\frac{1}{\rho}\right)^2 I_0 (U \sin \delta + V \cos \delta \cos \omega + W \cos \delta \sin \omega), \quad (4)$$

In Equation (4), where δ is the declination angle; ω is the solar hour angle; U, V, W represent the characteristic parameters related to geography and terrain. Equations to compute these factors were listed as following [6,64,96]:

$$U = \sin \varphi \cos \alpha - \cos \varphi \sin \alpha \cos \beta, \quad (5)$$

$$V = \sin \varphi \sin \alpha \cos \beta + \cos \varphi \cos \alpha, \quad (6)$$

$$W = \sin \alpha \sin \beta, \quad (7)$$

φ is the latitude, α is the slope of the study point, β is the aspect of the study point. The calibration coefficient of solar-Mars distance can be given by the Equation (6) of [2] or found in [9,10,27]:

$$\left(\frac{1}{\rho}\right)^2 = (1 + e \cos \theta) \div (1 - e^2)^2, \quad (8)$$

$$\theta = L_s - L_0, \quad (9)$$

where e (0.09377) is the eccentricity of Mars orbiter, L_s is the areocentric solar longitude, θ is the true anomaly of Mars, and L_0 is the areocentric longitude of Mars perihelion. Note that the value of L_0 was usually evaluated at 248° to calculate the calibration coefficient of solar-Mars distance in the previous even recent papers [2,3,10,27–30,41,103]. However, this was assessed by a much older study [104]. Then, it was improved to a moderately accurate estimate value: 250.99 (251°) [55,105]. It has been employed in a few previous research works [55,56,106–109] and employed in the Mars Climate Database (MCD), which is a database of atmospheric statistics compiled from state-of the art Global Climate Model (GCM) simulations of the Martian atmosphere. However, even now, many articles still use the 248° as mentioned above, thereby this paper proposed it.

The solar constant of Mars(or mean beam irradiance) [2]:

$$I_0 = I_{\text{solar}} \times (R_{\text{solar}} \div R_{\text{Mars}})^2 \quad (10)$$

where I_{solar} is the solar constant of Earth ($0.082 \text{ MJ} \cdot \text{m}^{-2} \cdot \text{min}^{-1}$ or $1371 \text{ KW}/\text{m}^2$, in this paper, we used $0.082 \text{ MJ} \cdot \text{m}^{-2} \cdot \text{min}^{-1}$) [2,6], R_{Mars} is the average distance from Mars to the sun; R_{solar} is the average distance from Earth to Sun [2].

The declination angle can be calculated by the spherical triangle law of cosines:

$$\cos(90^\circ - \delta) = \cos \varepsilon \cos 90^\circ + \sin \varepsilon \sin 90^\circ \cos(90^\circ - \theta), \quad (11)$$

where ε (25.19°) denotes the obliquity to orbit. According to [2], it can be simplified even further to:

$$\sin \delta = \sin \varepsilon \sin L_s, \quad (12)$$

However, since the rise and set of the sun, each Martian sol has a limited amount of PSD. and We present the PSD as an interval $[\omega_r, \omega_s]$.. Adding up the SASR for the PSD from sunrise to sunset, we can obtain the Equation for calculating one Martian sol's quantity of SASR on the sloped surface which is the integration of Equation (4) [6,14]:

$$Q_0 = \frac{T}{2\pi} \left(\frac{1}{\rho}\right)^2 I_0 \int_{\omega_{r1}}^{\omega_{s1}} (U \sin \delta + V \cos \delta \cos \omega + W \cos \delta \sin \omega) d\omega, \quad (13)$$

where ω_{r1} is the solar hour angle at the beginning of the PSD, ω_{s1} is the solar hour angle at the end of the solar hour angle, Q_0 denotes the daily SASR on the sloped surface from ω_{r1} to ω_{s1} ; T is the time of one Martian sol, i.e., 24.6230556×60 (in minutes).

ω_{s1} and ω_{r1} , i.e., the true sunrise and sunset on the incline plane can be obtained from equation 13-21 in [1]. The true beginning of the PSD and the true hour angle at the end of the PSD take into account of the hour angle of sunrise and sunset on the horizontal plane and the hour angle of sunrise and sunset on the inclined plane. The true sunrise should

be determined by which of the two sunrises occurs later and the actual sunset should be determined by which of the two sunsets occurs earlier [1,27,32].

However, this paper did not use the method of [1] to determine the true sunrise and sunset of PSD. The actual surface in DEM is rugged, not stationary incline (there is terrain relief in all directions). The rugged terrain may lead to the shielding effect. As we know, both the sun elevation angle and the sun azimuth angle vary with the time (solar hour angle), which cause the sun angle of incidence is different. Therefore, in each solar hour angle, SASR may be shielded by the terrain relief. The distributed model (or called subparagraph integral mathematical model) was generally adopted to calculate the actual SASR and PSD over the rugged terrain [6,8,11,12,14,15,17,64,96,97,109] in DEM. It was given in the following part.

2.2.3. Theoretical Equation for Calculating PSD and SASR on Rugged Terrain

SASRs are affected by the terrain relief at the total period of PSD. That is to say, in some subperiods of PSD for certain Martian sol, the study point may be shielded by the terrain relief and the subperiods of PSD should be zero. Thus, we should reconsider Equation (13). the general method in digital terrain analysis [6,8,11,12,14,15,17,64,96,97] is that we take horizontal sunrise and sunset angle as a value domain. Then, we cut this range into n small intercell. The 20 min were used as an intercell. We determine the shielding effect of the given position each 20 min. There are two methods to determine the shading status of the sample point in each intercell. One is by the ray tracing method [8] and the other is by the hillshade algorithm [109]. Then, we can get m periods of valid PSD: $[\omega_{sr1}, \omega_{ss1}, \dots, \omega_{srl}, \omega_{ssl}, \dots, \omega_{srm}, \omega_{ssm}] (l = 1, 2, \dots, m)$. The true sunset and sunrise should be the beginning of the first available PSD intercell and the end of the last valid PSD intercell. The general steps are given in the following:

- (1) ω_r and ω_s are the hour angle of sunrise and the hour angle of sunset on the horizontal plane, respectively. Their values, changing with the varies of points' location and time, can be given by:

$$\omega_s = \arccos(-\tan \varphi \tan \delta), \quad (14)$$

$$\omega_r = -\omega_s, \quad (15)$$

Note that the above Equation applies only to $|\varphi| < \pi/2 - |\delta|$. There are two special cases in which the above Equation is not applicable. Correspondingly, when $-\tan \varphi \tan \delta > +1$, The phenomenon of the polar night will occur, i.e., PSD should be zero. likewise, solar radiation should also be zero; When $-\tan \varphi \tan \delta < -1$, the phenomenon of the polar day will occur, i.e., PSD should be all day [1,2].

- (2) Using $\Delta\omega$ as a sun hour angle step length, the $[\omega_r, \omega_s]$ should evenly be divided into n intercell. For each intercell, we consider whether solar radiation is covered by surrounding terrain at the study point. Besides, there is a time step length denoted by Δt for each different $\Delta\omega$. $\Delta\omega$ can be given by:

$$\Delta\omega = \frac{2\pi}{24.6230556 \times 60} \times \Delta t, \quad (16)$$

n can be given by:

$$n = \text{int}\left(\frac{\omega_s - \omega_r}{\Delta\omega}\right) + 1, \quad (17)$$

where $\text{int}()$ is a function which can obtain the integral part of the $\left(\frac{\omega_s - \omega_r}{\Delta\omega}\right)$ Thus n intercell can be obtained:

$$\omega_i = -\omega_0 + \Delta\omega (i = 0, 1, 2, \dots, n - 1) \quad (18)$$

$$\omega_n = \omega_s, \quad (19)$$

- (3) Whether a point can be exposed to sunlight depends on the sun elevation angle and the azimuth angle and the shielding status function caused by surrounding terrain.

The sun elevation angle and azimuth angle of every intercell can be given by the following Equations:

$$h_i = \sin^{-1}(\sin \delta \sin \varphi + \cos \delta \cos \varphi \cos \omega_i), \quad (20)$$

$$A_i = \cos^{-1}[(\sin h_i \sin \varphi - \sin \delta) / \cos h_i \cos \varphi], \quad (21)$$

$$\text{Hillshade} = \cos(h_i) \times \cos(\alpha) + \sin(h_i) \times \sin(\alpha) \times \cos(A_i - \beta), \quad (22)$$

where h_i is the sun elevation angle; A_i is the azimuth angle; Hillshade is a function of the terrain shading status depending on which we can get the terrain shading factor for each different period. we denote terrain shading status factor as S_i where $S_i = 0$ indicates the study point was shaded and $S_i = 1$ indicates It was exposed to the sun. The hillshade algorithm, which was derived from and employed in the ArcGIS tool, was used to analyzes the local terrain shadow by considering the illumination source angle (solar incident angle) and surrounding terrain shadows. It is generally used to determine the assumed brightness value of a given position at a given time (solar altitude angle and solar azimuth angle vary with solar hour angle) influenced by the surrounding terrains. It has been used to determine the shielding status of solar radiation. [109–117]. The obtained value, which was named as hillshade value, ranges from 0–255. The corresponding Equation was

$$\text{Hillshade} = 255 \times \cos(h_i) \times \cos(\alpha) + \sin(h_i) \times \sin(\alpha) \times \cos(A_i - \beta), \quad (23)$$

The hillshade value ranges from 0–255. When hillshade > 0, the place is incident by sun; when hillshade = 0, the place is shielded by the terrain. In this paper, the hillshade was reclassified to terrain shading status factor as S_i according to Equation (22). When hillshade > 0, $S_i = 1$; when hillshade = 0, $S_i = 0$.

- (4) We now can calculate the PSD with considering the shielding effect. The PSD considering shielding effect should be obtained by adding up all the PSD subperiod which has available sunshine. Defining g_i as the shielding coefficient of each period which can be determined by the surrounding S_i :

$$g_i = \begin{cases} 1 & S_i = S_{i-1} = 1 \\ 0 & S_i = S_{i-1} = 0 \\ 0.5 & S_{i-1} = 1 \text{ and } S_i = 0, S_{i-1} = 0 \text{ and } S_i = 1 \end{cases} \quad (24)$$

The PSD of certain study point in the rugged terrains can be given by:

$$T_0 = \frac{24.6230556}{2\pi} \left(\sum_{i=1}^{n-1} g_i \Delta\omega + g_n \text{mod} \left(\frac{\omega_s - \omega_r}{\Delta\omega} \right) \right), \quad (25)$$

where $\text{mod}()$ is a function which can obtain the remainder part of the $\left(\frac{\omega_s - \omega_r}{\Delta\omega}\right)$. Hereafter, the PSD indicates the PSD which considers the terrain relief.

- (5) The SASR which considers the terrain relief effect is obtained by adding up the SASR in all available PSD. Whether a point can be exposed to sunlight in the integral part $[\omega_{i-1}, \omega_i]$ is determined by the S_{i-1} and S_i . If $S_i = 0, S_{i+1} = 0$ or $S_i = 0, S_{i+1} = 0$, nothing should be done in the $[\omega_i, \omega_{i+1}]$; If $S_i = 0, S_{i+1} = 1$, the angle of new PSD should begin as ω_{sr1} which was the mean value of ω_i and ω_{i+1} ; If $S_i = 1, S_{i+1} = 0$, the angle of new PSD should end as ω_{ss1} which was the mean value of ω_i and ω_{i+1} . Thus, an array of solar hour angles for an m segment can be obtained (in this array, the true sunrise and sunset solar hour angle over the rugged terrains should be the beginning of the first valid PSD and the end of the last valid PSD respectively):

$$[\omega_{sr1}, \omega_{ss1}, \dots, \omega_{sr1}, \omega_{ss1}, \dots, \omega_{srm}, \omega_{ssm}] (l = 1, 2, \dots, m) \quad (26)$$

We can obtain the daily SASR at the calculated point by adding up the SASR in the PSD which has available sunshine:

$$W_0 = \frac{T}{2\pi} \left(\frac{1}{\rho}\right)^2 I_0 \left[U \sin \delta \sum_{i=1}^m (\omega_{ssl} - \omega_{srl}) + V \cos \delta \sum_{i=1}^m (\sin \omega_{ssl} - \sin \omega_{srl}) - W \cos \delta \sin \omega \sum_{i=1}^m (\cos \omega_{ssl} - \cos \omega_{srl}) \right] \quad (27)$$

where W_0 denotes the SASR for one certain Martian sol, other parameters see above.

2.2.4. Calculation of PSD and SASR for Each Martian Sol, Season, and One Year

To calculate SASR on Mars for different Martian days, we should compute the declination δ and areocentric longitude L_s for each Martian sol. Two methods to obtain the relationship between the Martian sols and the areocentric solar longitude were given in this paper. They were given as follows:

Method 1: the first method was based on Kepler's equation. It was firstly proposed by Johannes Kepler in 1609 to reflect the function relationship between the position of the planet on the planetary orbit and the corresponding solar time. For a given sol number T_n , the corresponding value of areocentric solar longitude L_s maybe calculated by Kepler's equation. To recapitulate briefly, it can be calculated by the following two steps:

Step 1: Establishing the Kepler's equation as:

$$M = E - e \sin E, \quad (28)$$

where M is the mean anomaly, E is the eccentric anomaly. The mean anomaly M is related to sol numbers by:

$$M = 2\pi \frac{T_i - T_p}{T_s}, \quad (29)$$

where T_i is the sol number, T_s is the number of sols in a Martian year (668.6), T_p is the perihelion date: 485.35. Then, under the Equation (28) and (29), for each T_i , the corresponding E can be obtained. Noted that the solutions were usually dissolved by Newton iterative method which may yield an identical solution to Kepler's solution.

Step 2: calculations of the true anomaly:

Geometrically, the eccentric anomaly E and the true anomaly θ have the following relationship:

$$\cos E = \frac{e + \cos \theta}{1 + e \cos \theta}, \quad (30)$$

$$\sin E = \frac{\sqrt{1 - e^2} \sin \theta}{1 + e \cos \theta}, \quad (31)$$

Then, the relationship between θ and E can be further simplified to:

$$\theta = 2 \arctan \left[\sqrt{\frac{e+1}{1-e}} \tan \left(\frac{E}{2} \right) \right], \quad (32)$$

Step 3: calculations of the areocentric solar longitude L_s :

$$L_s = (\theta + L_0) \bmod(360), \quad (33)$$

Method 2: the second method was based on Kepler's second law: a line joining a planet and the Sun sweeps out equal areas during equal intervals of time. It can be denoted by the Equation below:

$$\frac{T_i}{T_s} = \frac{\int_0^\theta \int_0^{\frac{a(1-e^2)}{1+e \cos \theta}} \rho d\rho d\theta}{\pi ab}, \quad (34)$$

where a is the Mars semi-major axis, b is the Mars semi-minor axis. Other parameters see the papers above. Then, for each T_i , the corresponding θ can be obtained by the

above Equation (34). Under the Equations (33) and (34), the corresponding L_s can both be calculated.

For the above two methods, we calculated separately, and the result seemed little different (the ratio of result for the first method to the second method was between 0.999871–1.00081). In this paper, we adopted the first method to calculate the corresponding L_s for each Martian sol.

The duration division on Mars, shown in Table 2, was different from the Earth due to the difference of orbit and speed between Mars and Earth. In this paper, referring to the MCD' s standard, the areocentric solar longitude was equal divided into 12 classes. Each areocentric solar longitude class corresponds to a Martian month and every three months corresponds to a season as shown in Table 2. For each sample area, using twenty minutes as a unit, we calculated the value of PSD and SASR for each twenty minutes in one Martian sol. Then, we obtained the PSD of each Martian sol by adding up the SASR and PSD of all the corresponding twenty minutes in one sol. Similarly, the PSD and SASR in each season were obtained by adding up the PSD and SASR of the days in each season. Ultimately, we can obtain the SASR and PSD for one year by adding up the SASR and PSD for 669 Martian sols.

Table 2. The Martian durations in different month number.

| Month Number | Solar Longitude Range (in Degree) | Duration (in Sols) |
|--------------|-----------------------------------|--------------------|
| 1 | 0–30 | 61 |
| 2 | 30–60 | 66 |
| 3 | 60–90 | 66 |
| 4 | 90–120 | 65 |
| 5 | 120–150 | 60 |
| 6 | 150–180 | 54 |
| 7 | 180–210 | 50 |
| 8 | 210–240 | 46 |
| 9 | 240–270 | 47 |
| 10 | 270–300 | 47 |
| 11 | 300–330 | 51 |
| 12 | 330–360 | 56 |

2.3. Method for Extracting the Roughness-Mean SASR Spectrum and Roughness-Mean PSD Spectrum.

2.3.1. Extraction of Roughness

Slope has been proven to be a parameter which is a significant methodology in revealing features of SASR on Earth to some extent [12]. It is also an efficient method to reveal the relations between terrain and SASR [11,24]. However, since the limitations of MOLA data (the latest available data is not a high-precision one), the microcosmic terrain factor (i.e., slope) may be not an available factor to be employed on Mars for revealing the influences of terrain relief to SASR in different topography. A low resolution of the data will result in lower mean value and standard deviation of slope information [118]. That is, if we use slope to describe terrain relief in the resolution of 200 m, the terrain feature information may be single and inaccurate. This was also verified by our experiments. We selected 50 random sample areas to calculate their slopes. For each sample areas, the extracted average slope is generally less than 10 degrees and standard deviation is generally less than 8, which proves that slope is not suitable for the study of the terrain analysis of SASR on Mars. Accordingly, we should find an efficient macro terrain factor to replace the slope to reveal the terrain relief of Mars. In topographic statistical analysis, roughness was generally used together with slope to describe terrain relief. It may be a proper parameter to displace the slope which has been employed in many planetary theories to reveal the terrain relief including Mars and the moon [73,81,119–125].

There are numerous representative models to quantize the roughness on the surface. They can be divided into surface area ratio model [126], vector ruggedness model [127–129],

surface roughness factor based on the delta transformation of slope and aspect [129,130], commonly reported models based on statistical theory (the Hurst exponent, root-mean-square height, root-mean-square slope, height distribution deviation, autocorrelation length, median and absolute slope, etc.) respectively [125,130]. The method to quantitatively characterize surface roughness will differ according to different application purposes. The quantification of local topographic relief is usually simulated by using statistical theoretical parameters. In the statistical analysis of roughness, root-mean-square height (RMS) was a high-frequency parameter. RMS, which was generally considered as a proper parameter to describe roughness in statistical analysis, were used to produce the global roughness surface maps of Mars and analyze local terrain relief on Mars and the moon [81,119,121,123–125]. It seemed to show a good ability to reveal the local terrain relief on the surface [118–120,123,131]. It was also used to classify different geological units [73,122]. Furthermore, it has proven to have a good ability to reveal characteristics of slope variation and local terrain variation [132]. Thus, in this paper, we use RMS to quantize the local terrain relief. It can be calculated by the following Equation:

$$\rho = \sqrt{\frac{1}{n-1} \sum_{i=1}^n (h(x_i) - h_{\text{mean}})^2}, \quad (35)$$

where n is the number of sample points in the local analysis window, $h(x_i)$ is the height of the center sample point of the analysis window, and h_{mean} is the average height of all the observed sample points. In general, the rugged the surface, the larger RMS is.

Since the RMS has scale dependence, the choice of the right step size is critical. Note that the appropriate scale varies according to our algorithm for SASR affected by topography. The terrain algorithm can be divided into in hillshade algorithm which is both used in Arc/Info and Genasys [109–116] and the ray-tracing method. When using the ray-tracing method, the appropriate scale of the calculated terrain factor should vary with the search radius of the ray-tracing method. In this paper, considering that the data resolution is 200 m (in meter), which is not the high-resolution data, we adopted the hillshade algorithm. On the other hand, the hillshade algorithm determines the shielding effect of each grids according to the eight points around the grid points [109,113,116]. That is, when using hillshade algorithm, we consider the terrain relief of the 8 sample points around the sample points, so the local terrain relief revealed by our topographic factor should also be the terrain relief around the sample points exposed. Thus, when we use roughness to reveal the local terrain relief, the proper scale for roughness should be consistent with the analysis sample window of the hillshade algorithm. The analysis window of hillshade algorithm is a 3×3 grid (each grid is a 200×200 m grid). i.e., the proper scale for roughness is the range of $600 \text{ m} \times 600 \text{ m}$.

2.3.2. Extracting Procedure of the Stable Roughness-Mean Shielded Astronomical Solar Radiation Spectrum

The SASR spectrum can be viewed as a group of SASR histogram under certain grading laws based on one certain terrain factor. In this paper, we used RMS as a parameter in the x-axis; i.e., the SASR spectrum was a group of SASR histogram under certain grading laws based on RMS. Likewise, the PSD spectrum is a group of PSD histogram under certain grading laws based on RMS. A specific geomorphic type has its own characteristic SASR and PSD spectrum curves. The validity of the spectrums lies on whether the spectral sample region of the spectrum we used to extract is greater than the critical area threshold. When the spectral sample region of the sampling area is greater than the critical area threshold, the characteristic spectral curve shows a stable trend, and vice versa (see Figures 1 and 2). The spectrum whose spectral region is greater than the critical area is considered as the stable roughness-mean SASR spectrum of the landform and the stable roughness-mean PSD spectrum of the landform, respectively. For convenience, the stable roughness-mean SASR spectrum may be called *RS* hereafter. Furthermore, the critical area of *RS* may be called X_1 . Similarly, the stable roughness-mean PSD spectrum may be called *RP* in the

following paper for brevity. Then, the critical area of *RP* may be called X_2 . The technical route to extract *RS* and *RP* is given in Figure 3.

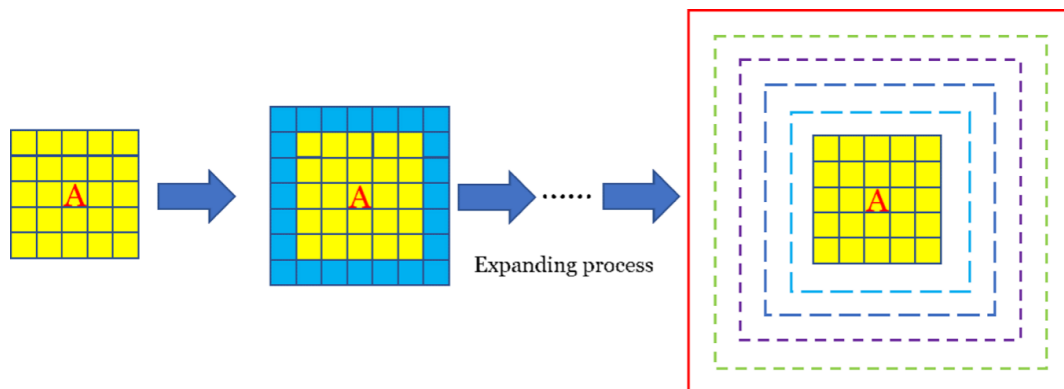


Figure 1. The gradual expanding process of the spectrum. Grid A is the center of the analysis window. This yellow window consist of 5×5 grids is the initial analysis window. Then, it expands the periphery area to be a new rectangular window whose shape is 7×7 . When the quantitative indicators of similarity do not meet the abovementioned conditions, it will continue to expand. As we can see, it is a gradual process: The window size goes from 5×5 to 7×7 to $9 \times 9 \dots$

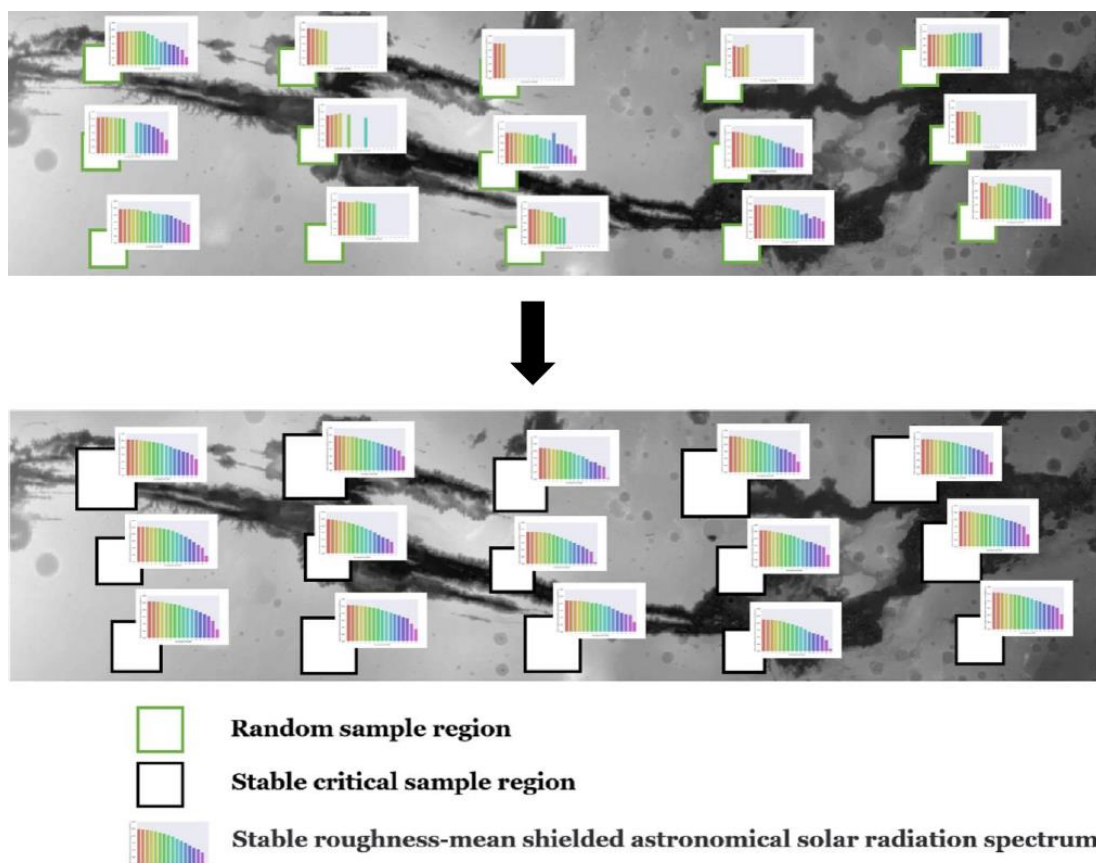


Figure 2. 80 random grid points were selected to yield the spectrums in Valles Marineris. When the area of the extracted analysis window was less than the critical area (the green sample window), the spectrums showed the characteristics of the unstable disorder. Afterwards, along with the increase of analysis windows size, the spectrums gradually show a certain similarity and stability. Finally, when the area of the extracted analysis window was greater than the threshold of the critical area (the black sample window), the spectrums all showed a stable trend. Besides, the extracted analysis windows whose area is greater than the threshold of the critical area were all regarded as the stable area, which is because the extracted spectrums generally showed a certain similarity and stability.

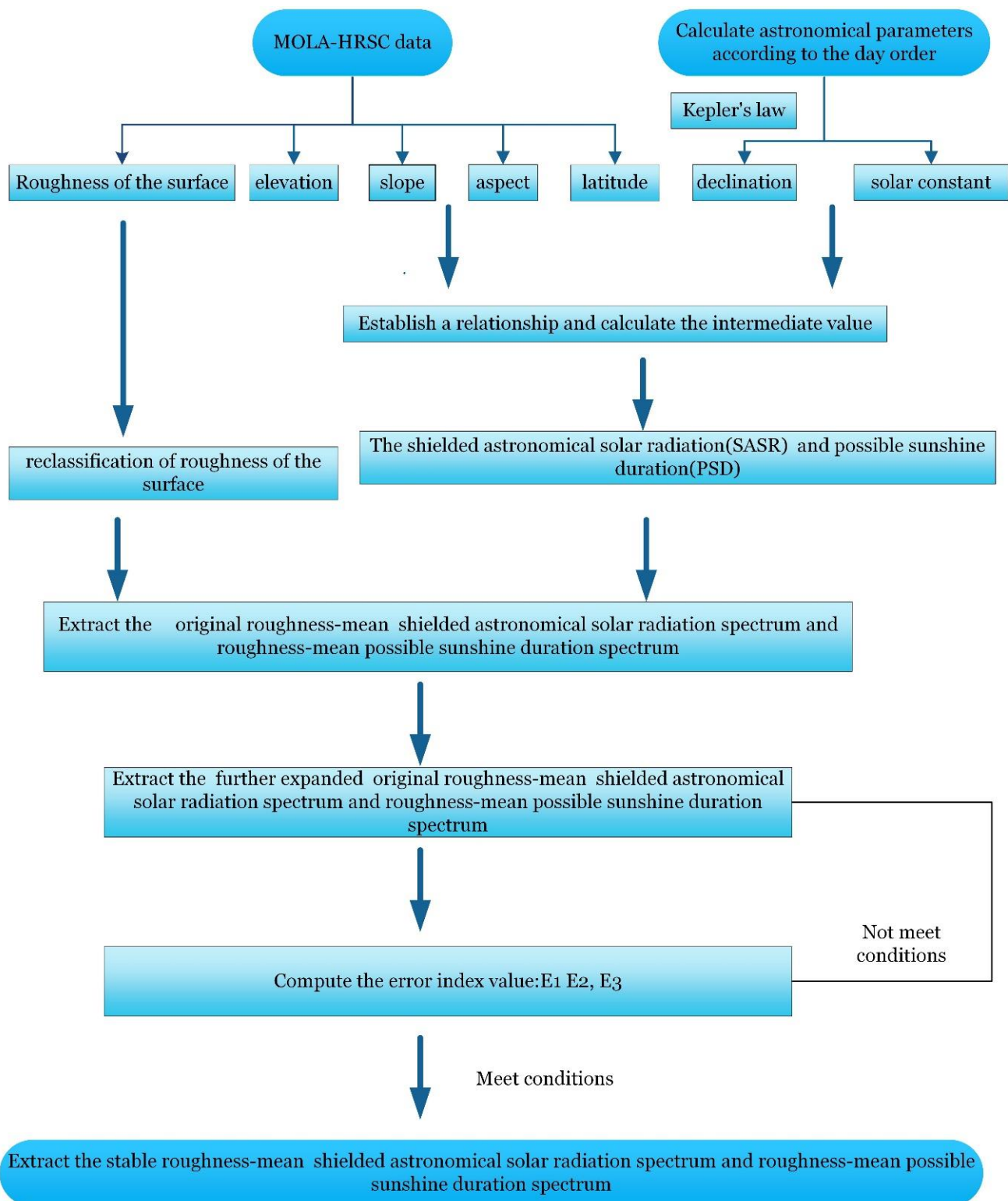


Figure 3. Technical route to extract the roughness-mean shielded astronomical solar radiation spectrum and roughness-mean possible sunshine duration spectrum. The roughness was reclassified by root-mean-square (RMS). The declination and solar constant for each day order calculated from Kepler's law can be employed to calculate the calibration coefficient of solar-Mars distance (see Equations (8) and (9)) which is the intermediate value of the calculations for shielded astronomical solar radiation (SASR) and possible sunshine duration (PSD) on rugged terrains. Then, the final Equation (see Equation (27)) established the relationship between the terrain factors and astronomical parameters under the distributed model proposed in Section 2.2.2.

In every spectral sample region, SASR was divided into 17 classes according to RMS by using equal-interval RMS classification (The 17 RMS classes respectively were: 0–5 m, 5–10 m, 10–15 m, 15–20 m, 20–25 m, 25–30 m, 30–35 m, 35–40 m, 40–45 m, 45–50 m, 50–55 m, 55–60 m, 60–65 m, 65–70 m, 70–75 m, 75–80 m, 80 m–). That is, the SASRs of the grids whose RMS was in the same class were averaged to be one value. Then, the corresponding 17 values obtaining from each class became a group. The initial spectrum can be denoted as a group of histogram: $RS_1 = \{S_1, S_2, S_3, S_i, \dots, S_n\}$, where i is the number of roughness classes and S_n denoted the mean SASR values of grids belonging to the same RMS class.

The spectrum method reveals the similarity of nearby terrains. We defined the quantitative indicators of similarity as $\&_1$, $\&_2$ and $\&_3$. The quantitative indicators of similarity $\&_1$ and $\&_2$ can be calculated by $\&_1 = \text{Max}\left(\left|\frac{RS_1 - RS_2}{RS_1}\right|\right)$ and $\&_2 = \sum_{i=1}^n |(RS_1 - RS_2)/RS_1|$ respectively, where RS_1 denoted the spectrum before expansion, RS_2 denoted the spectrum after expansion. $\&_3$ is an auxiliary parameter, which requires that the grids in the spectral sample region have a least one value in each RMS class. They were employed to determine whether the roughness-mean SASR spectrum before expanding is stable.

The process of obtaining the critical area is an expanding process. The gradual expanding process of the spectral sample region is presented in Figure 1. The initial spectral sample region was a rectangular analysis window of 5×5 . We chose a random grid in the sample area as the center of the analysis window. The roughness parameter (RMS) of each grid in the analysis window was calculated as mentioned in Section 2.3.1 and classified into 17 classes. The SASR of each grid in the spectral sample region was also calculated as the method mentioned in Section 2.2. Then, we added up the SASR values of grids belonging to the same RMS class and calculate the mean value, respectively. The initial spectrum, i.e., a group of the histogram in a coordinate whose x-axis is the classified RMS and y-axis is the mean SASR of grids belonging to the same RMS class, was obtained.

The initial spectral sample region of specific landform was constantly expanded, and the quantitative indicators were constantly calculated until there are thirty continuous expanding spectrums that satisfy the $\&_1 < 0.001$, $\&_2 < 0.001$, $\&_3$. When the continuous thirty expanding spectrums satisfied the corresponding conditions, we regarded that the spatial structure of spectrums from the first spectrum tends to be stable (i.e., under the limitations of $\&_1$ and $\&_2$, the corresponding spectrums derived from adjacent locations reach the similarity of 99.9%) The spectrum which was constructed by the first spectrum was regarded as RS . The area of the current spectral sample region based on the first spectrum was considered as the critical area of RS (i.e., X_1).

However, if it does not meet the conditions, the current spectral sample region should continue to gradually extend until $\&_1$, $\&_2$ and $\&_3$ meet the conditions. That is, when the area of the spectral sample region increased, the spectrum constructed by the current spectral sample region will be closer to the stable spectrum.

After the process of expanding under the limitations, we can obtain the RS , which is a group of the histogram: $RS = \{S_1, S_2, S_3, S_i, \dots, S_n\}$, where i is the number of roughness classes and S_n denoted the mean SASR values of grids belonging to the same RMS class (as seen in Figure 2).

Similarly, we can extract the stable roughness-mean PSD spectrum and obtain the critical area of RP (i.e., X_2).

2.3.3. Extracting Procedure of the Standard Stable Roughness-mean Shielded Astronomical Solar Radiation Spectrum

More tests, presented in Figure 2, were conducted to verify the feasibility of the stable roughness-mean SASR and PSD spectrum. Referring to the method of [77,79], random functions were taken to select 80 grids in all sample areas as the center of the analysis windows. These grids were used to yield 80 roughness-mean SASR spectrum and roughness-mean PSD spectrum, respectively. As presented in Figure 4, these spectrums showed the same trend and stability, which prove the stability and self-similarity of the extracted stable spectrums to some extent. In this paper, the coefficient of variation (COV)

and average relative error (ARE) were used to reflect the statistical dispersion of 17 RMS classes. Furthermore, the correlation coefficient (CORREL) and covariance were used to reflect the similarity of spectral curves. The calculation of correlation coefficient and covariance were not discussed in this paper due to the limited space. We counted 17 RMS class values of 80 spectral curves respectively. The calculation Equation of the COV and ARE is as follows:

$$COV_j = \sqrt{\frac{1}{80} \sum_{i=1}^{80} \left(S_{ij} - \frac{1}{80} \left(\sum_{i=1}^{80} S_{ij} \right) \right)^2} / \frac{1}{17} \left(\sum_{i=1}^{80} S_{ij} \right) \quad (j = 1, 2, 3, \dots, 17), \quad (36)$$

$$ARE_j = \frac{1}{80} \sum_{i=1}^{80} \left(S_{ij} - \frac{1}{80} \left(\sum_{i=1}^{80} S_{ij} \right) \right) \quad (j = 1, 2, 3, \dots, 17), \quad (37)$$

where j is the number of RMS class, i is the number of spectrum curve. The further the coefficient of variation is from zero, the greater the statistical dispersion of the data is. Within each RMS class, the COV of sample area at different durations (spring, summer, autumn, winter) are within the range of 0.01 to 0.11623; besides, within each RMS class, the ARE of sample area at different durations (year, spring, summer, autumn, winter) are ranging from 0.002% to 9.21%. The CORREL of 12 regions at different durations (year, spring, summer, autumn, winter) are ranging from 0.80212 to 0.9999 and 98% of the values are greater than 0.90; besides, the covariance is generally greater than 0, which indicated that the RS and RP invariably have the same trend. Consequently, we concluded that there are sufficient stability and similarity in the extracted stable PSD spectrums and SASR spectrums.

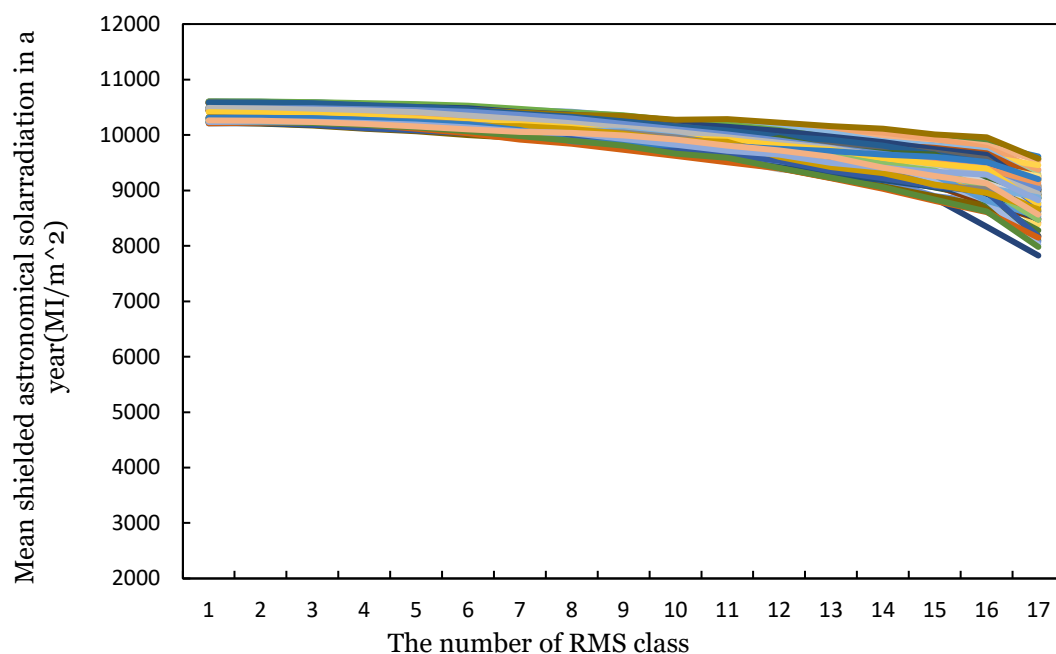


Figure 4. Stable roughness-mean shielded astronomical solar radiation spectrums of the different 80 regions in the sample area of Valles Marineris in a year. The roughness within sample windows was described by RMS and equally classified into an arithmetic progression (in meters): 0–5 m, 5–10 m, 10–15 m, 15–20 m, 20–25 m, 25–30 m, 30–35 m, 35–40 m, 40–45 m, 45–50 m, 50–55 m, 55–60 m, 60–65 m, 65–70 m, 70–75 m, 75–80 m, 80 m–. Noted that the grid with RMS which were greater than 80 m account for less than 6% of the total area in all sample areas, so we treat the interval which is greater than 80 m as a separate class. The stable spectrums, extracted in 80 regions separately, were presented in the figure. All spectral curves are distributed in a band and have the same trend and distribution. This showed a self-similarity and stability of the spectrums. Due to the paper’s space constraints, only the spectrums of Valles Marineris were given in the figure.

Given the local spectrum may not reflect the overall trend of SASR distribution in the sample area, to assess the extent of SASR and PSD affected by the terrain relief of the whole test area in a statistical sense, the standard SASR and PSD spectrum should be considered [76–80]. The standard spectrum was generally defined as the average of the extracted spectrum. In this paper, we defined the standard roughness-mean SASR spectrum as $R_S S$. $R_S S$ was obtained by averaging the extracted 80 RS. The RS in each sample area was denoted as $RS = \{S_{1,j}, S_{2,j}, \dots, S_{i,j}, \dots, S_{17,j}\}$ where i is the number of RMS classes, j is the number of divided areas. As such $R_S S$ can be expressed as the following equation:

$$R_S S = \left\{ \frac{1}{80} \sum_{j=1}^{80} S_{1,j}, \frac{1}{80} \sum_{j=1}^{80} S_{2,j}, \dots, \frac{1}{80} \sum_{j=1}^{80} S_{17,j} \right\} \quad (38)$$

Similarly, we defined the roughness-mean PSD spectrum as $R_S P$ and calculated it by averaging the extracted 80 RP.

We defined the standard X_1 as X_{1s} and the standard X_2 as X_{2s} . They were the maximum extracted critical area of the extracted 80 RS and RP respectively.

3. Results

3.1. Characteristics of Annual Spectrums

The extracted $R_S S$ and $R_S P$ for 12 sample areas in a year are shown in Figures 5 and 6, and the corresponding X_{1s} and X_{2s} are presented in Figure 7. $R_S S$ and $R_S P$ showed the specific spatial structure of SASR and PSD for each sample area. They were generally affected by the surrounding terrain and the position of latitude, which can be divided into the following two respect to be discussed.

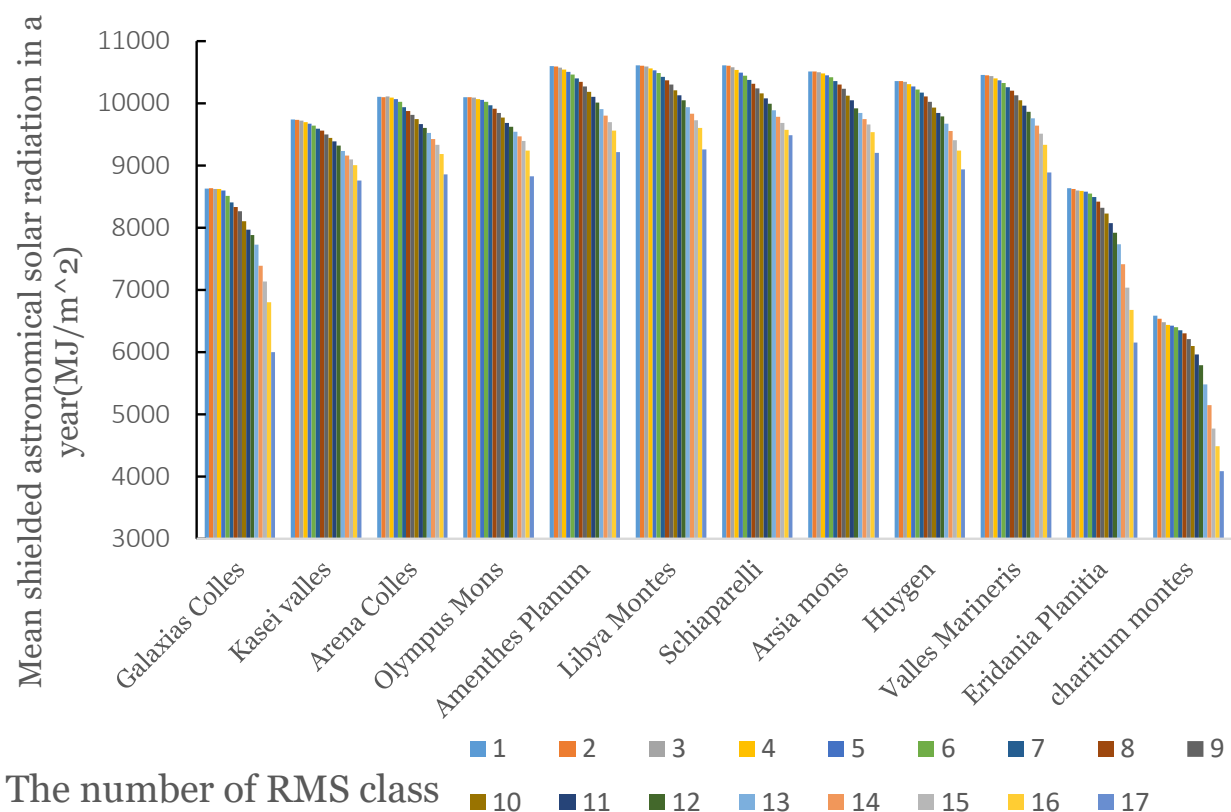


Figure 5. Roughness-mean shielded astronomical solar radiation spectrums of 12 sample area. The sample areas in this figure are sorted by latitude from left to right (39.07° N–58.1° S).

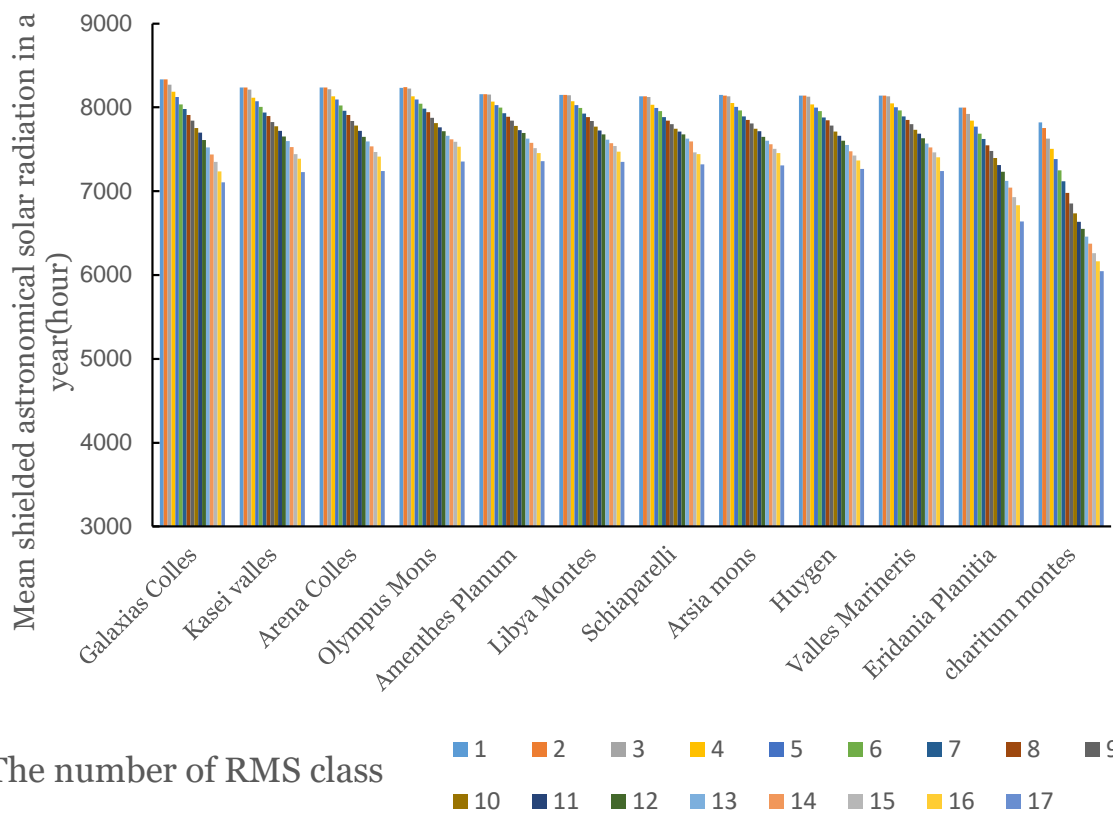


Figure 6. Roughness-mean possible sunshine duration spectrums of 12 sample areas. The sample areas in this figure are sorted by latitude from left to right (39.07° N– 58.1° S).

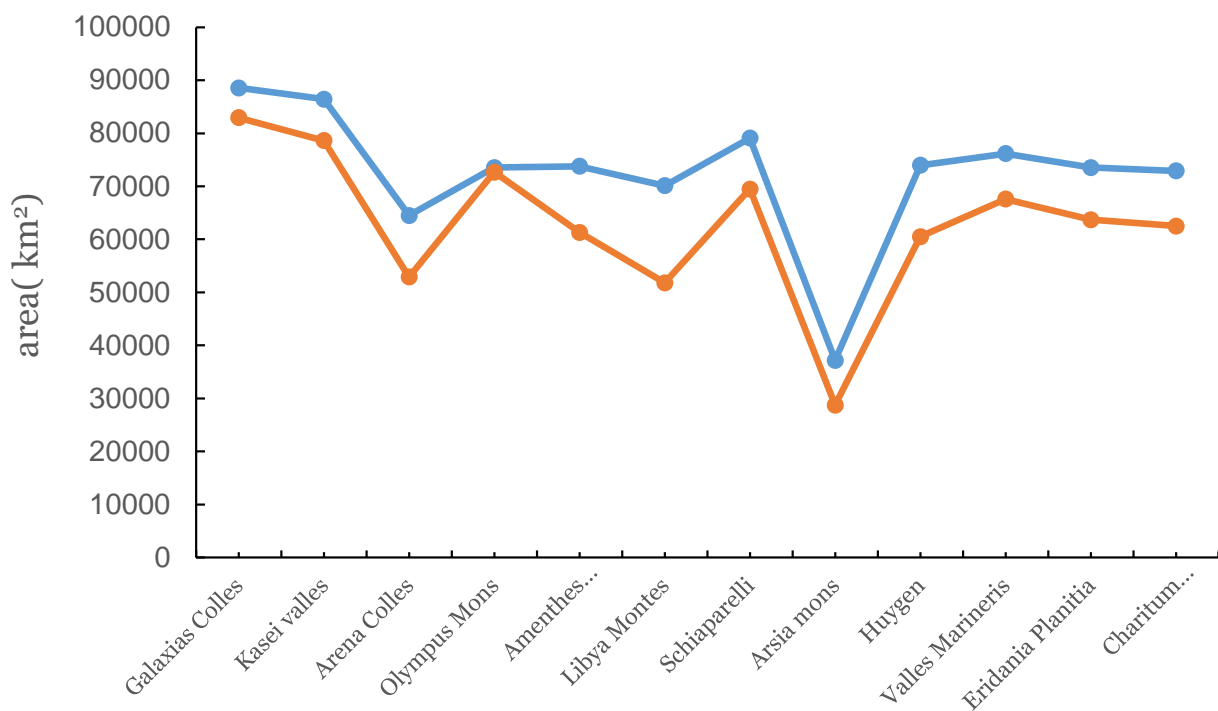


Figure 7. The value of critical areas of roughness-mean shielded astronomical solar radiation spectrums in a year of 12 sample areas and the critical area of roughness-mean shielded possible sunshine duration spectrums in a year of 12 sample areas. The blue curve is the former. The red curve is the latter. As seen in the figure, the critical area of R_{5S} was generally greater than that of R_{5P} .

3.1.1. The Law of Gradual Variation of R_{5S} and R_{5P} with Terrain Relief in Annual Spectrum

Result 1. We found that, for the same landforms, within each RMS class in R_{5S} , the value of SASR was generally different, which suggested that SASR showed different characteristics in different topographic conditions under the same landform. This law was also found in the PSD in R_{5P} .

Besides, in R_{5S} and R_{5P} , along with the increase of RMS classes, the value of SASR and PSD showed the same trend, i.e., they were generally decreased (see Figures 5 and 6). This can be explained by the following. Roughness is a parameter that can reveal the terrain relief of the given area. The greater the roughness, the more rugged the terrain. Then, the more rugged terrain may lead to a greater shielding effect than the less rugged terrain especially the flat surface. The shielding effect may generally cause the PSD and SASR to decrease. This finding seemed to be similar to the features of SASR and PSD found on Earth [6,8,12,14,64]. And it provided deep support for the conclusion: the region possessing complex terrain may generally have a strong terrain shielding effect.

That is, the SASR and PSD were influenced by terrain relief, either on Mars or Earth.

3.1.2. The Law of Critical Area with Terrain Relief

Result 2. We investigated the value of X_{1s} and X_{2s} found in 12 sample areas, which seemed to show the same descending order (see Figure 7). Furthermore, the value of X_{1s} was generally greater than X_{2s} (see Figure 7). That is, it seemed that a certain of similarities exist on the occurrence of the S_1P and S_2P ; and the variation of SASR is larger than PSD so that a larger critical area is needed to ensure the stability of the obtained spectrum.

Whether the critical area can be obtained depends on whether the landform has enough topographic feature information. For complex landforms, the topographic feature information will also be more complex, which further cause the corresponding spatial distribution of SASR to become more complex. The more complex spatial distribution of SASR may bring more topographic feature information, which leads to the larger X_{1s} . Accordingly, we may draw an inference: the value of critical area may be related to the complexity of topography. The variation coefficient of RMS described the variation of the terrain relief. Then, we found that a positive relationship seemed to exist between the value of X_{1s} and the variation coefficient of RMS (see Figure 8). This feature was also found in X_{2s} (see Figure 9). Furthermore, the following Equations were given in the test of 12 sample areas:

$$y = 80638 \times \ln(x) + 45212 \quad R^2 = 0.7062 \quad (39)$$

$$y = 77238 \times \ln(x) + 55699 \quad R^2 = 0.7804 \quad (40)$$

where x is the value of the variable coefficient of the RMS in each sample area and R^2 the correlation coefficient. The above Equations may reveal that the value of the critical area is generally positively correlated with the variation coefficient of RMS. The variation coefficient of RMS described the variation extent of the terrain relief. When it increased, the terrain relief may become complex. Then, the complex terrain relief may lead to a complex shielding effect which may cause the distribution of SASR and PSD more complex. Then, a larger critical area is needed to ensure the stability of the obtained spectrums. Namely, the more complex terrain generally meant the higher X_{1s} and X_{2s} .

3.1.3. Latitude Anisotropy Characteristics Influenced by the Shielding Effect in R_{5S} and R_{5P}

Result 3. Afterwards, we investigated that the R_{5S} usually showed an intimate relationship with the latitude of the site. As seen in Figure 5, for R_{5S} in the sample areas, with the latitude of the sample area decreasing, the SASR for each RMS class increased. The closer the sample area to the equator, the greater the SASR for each RMS class. This characteristic can be explained by the following. The lower the latitude, the higher the altitude angle of the annual mean midday sun (explained in Figure 8), and thus the

weaker the shielding effect of the sample area. The weaker shielding effect may result in greater SASR.

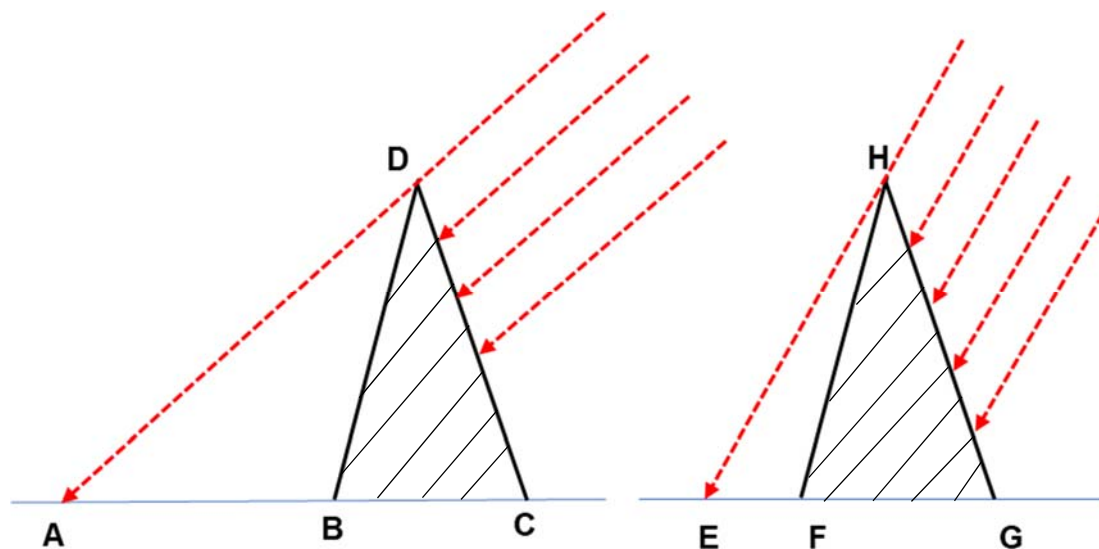


Figure 8. Shading conditions vary with the sun elevation angle. The polygonal BCD and HFG represent the same surface object in the sample area, DAC represents the sun elevation angle, HEG represents the higher sun elevation angle compared to DAC. When the DBC is directly illuminated by the sunbeam at the sun elevation angle of AD, BCD becomes a shelter to result in the shielding effect. The shielding effect causes the surface of AB to be unable to receive PSD. Obviously, as the sun elevation angle increased, the surface area which cannot receive the PSD decreased (varied from AB to EF). This figure reveals that the increase of the sun elevation angle may result in the weaker shielding effect.

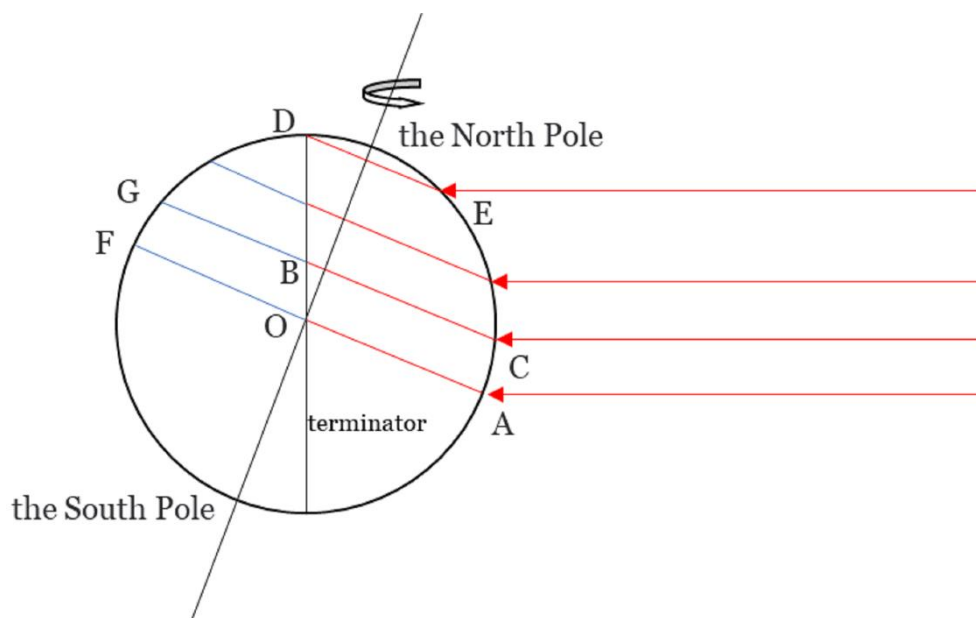


Figure 9. Variations of the duration of daytime with the increase of latitude in the northern hemisphere. AO, CB and DE respectively represent the day arcs at three regions in different latitudes (the corresponding latitude area AF, CG and ED respectively). AF is the equator and ED is the Arctic Circle. When sun directly illuminates the northern hemisphere (From vernal equinox to autumnal equinox), with the increase of the latitude, the proportion of the day arc to the circumference of latitude gradually increases. Until the latitude increased to Arctic Circle, the day arc accounted for 100% of the circumference of latitude. The ratio of day arcs to latitude is the ratio of daytime to one Martian day. That is, the duration of daytime increase with the increase of the latitude of the sample region.

As presented in Figure 6, the same characteristics were also shown in $R_S P$ of the sample area in the southern hemisphere. However, we found that in the northern hemisphere, the PSD showed the contrary characteristics. That is, for $R_S P$ in the sample area of the northern hemisphere, with latitude increasing, the PSD generally increased. This characteristic may be because of the imbalanced seasons caused by Martian moving orbits and velocity (see Table 1). The unique Martian orbits and velocity influenced its revolution and rotations, which result in the corresponding time laws. It may be explained as follows. Because of the obliquity of the ecliptic, the sun can illuminate only half of the Earth, which was divided by the terminator. When the sample area in the northern hemisphere is in spring and summer, the daytime which is from sunrise to sunset may become longer with the latitude increasing (see the corresponding explanation in Figure 9). Besides, with latitude increasing, the shielding effect may gradually enhance. Generalizing these two factors, with latitude increasing, the PSD in spring and summer may increase. Similarly, we may infer that with latitude increasing, the PSD in the northern hemisphere in autumn and winter may become decrease. Then, the unique Martian movement causes the days of spring and summer on Mars are much longer than that of autumn and winter (the ratio of the durations for each season is 1.34: 1.25:1: 1.08, while it is nearly 1:1:1:1 on Earth), which may lead to the result that the increase of PSD in spring and summer is greater than the decrease of PSD in autumn and winter. Thus, the PSD in the northern Martian hemisphere in a year, which was calculated by adding up the PSD of four seasons, may increase with the increase of latitude.

Additionally, the above result seemed to show that SASR is more sensitive to the shielding effect than PSD because it showed sufficient regularity under the influence of the shielding effect.

Result 4. Another investigation is that the descending rates of SASR in $R_S S$ and PSD in $R_S P$ are affected by latitude (see Figures 10 and 11). In $R_S S$ and $R_S P$, the relationship between SASR, PSD and roughness classes may be generally denoted as a linear relationship: $y = a_n x + b$, which y denotes the value of SASR or PSD, x denotes the number of roughness classes and the R^2 is ranged from 0.9012–0.998. a_n is generally negative, representing a decreasing trend of SASR and PSD with the increase of roughness classes, which may provide support for result 1. Then, we found that, as seen in Figures 10 and 11, along with latitude decreasing, the a_1 and a_2 for SASR and PSD respectively, seem to generally increase. The closer the sample area to the equator, the greater a_n . The explanation for this conclusion is an inference from the previous conclusion. According to result 2, with the decrease of latitude, the sun elevation angle may increase, resulting in a weaker shielding effect in $S_S P$. Besides, the decay rate of the SASR (a_1) and PSD curve (a_2) represented a variation rule of SASR and PSD under the influence of topographic relief. As the shielding effect weaken, the PSD within each RMS class will approach the ideal value of PSD (the latter did not consider the shielding effect and was a constant value, i.e., the PSD in the length of the daytime from sunrise to sunset). The smaller the latitude, the closer the values in each RMS class are to the same value. That is, as the latitude decreases, a_2 may become gradually greater, which represents the continuous decrease of the decay rate. The explanation for the increase of a_2 with the decrease of latitude can be given in a similar way provided for a_1 .

Furthermore, we found that a_1 was generally less than a_2 (see Figures 8 and 9). It meant that the attenuation rate of PSD with topographic relief is lower than that of SASR under the same terrain shielding condition. This finding may further provide support for the inference in result 3 that SASR is more sensitive to the shielding effect than PSD.

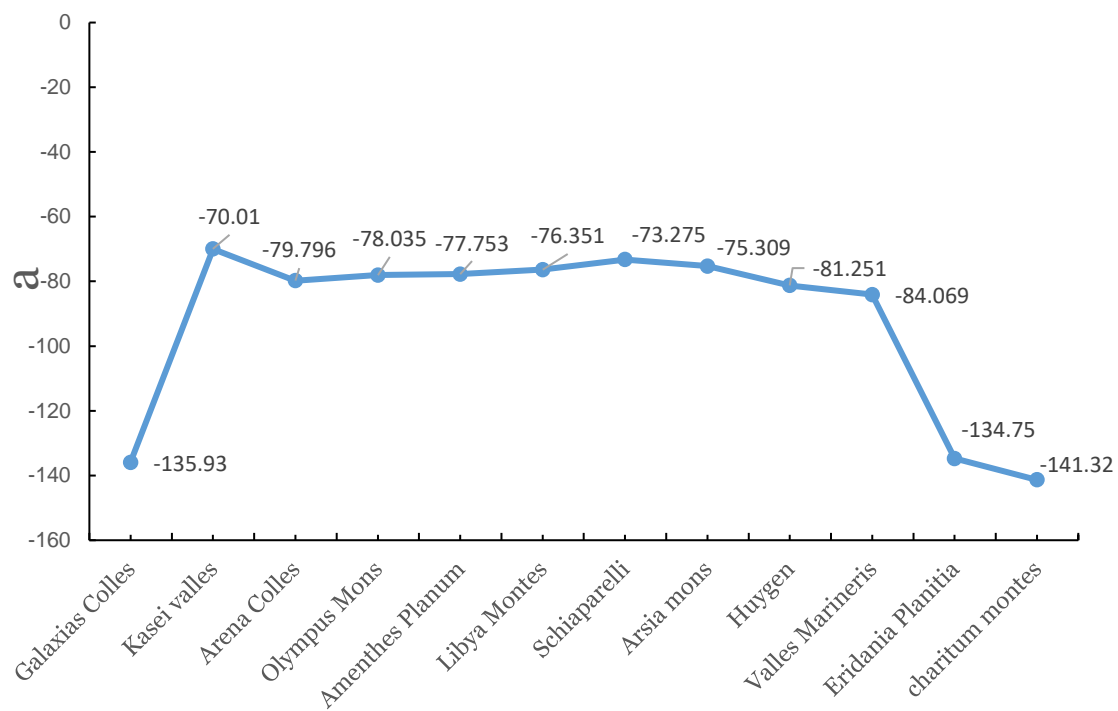


Figure 10. The descending rate of SASR is affected by latitude. The sample areas in this figure are sorted by latitude from left to right (39.07° N– 0° – 58.1° S). The descending rate of SASR and PSD showed the same trend: from the northern hemisphere to the equator, the rate became slower; Then, from the equator to the southern hemisphere, the rate becomes faster.

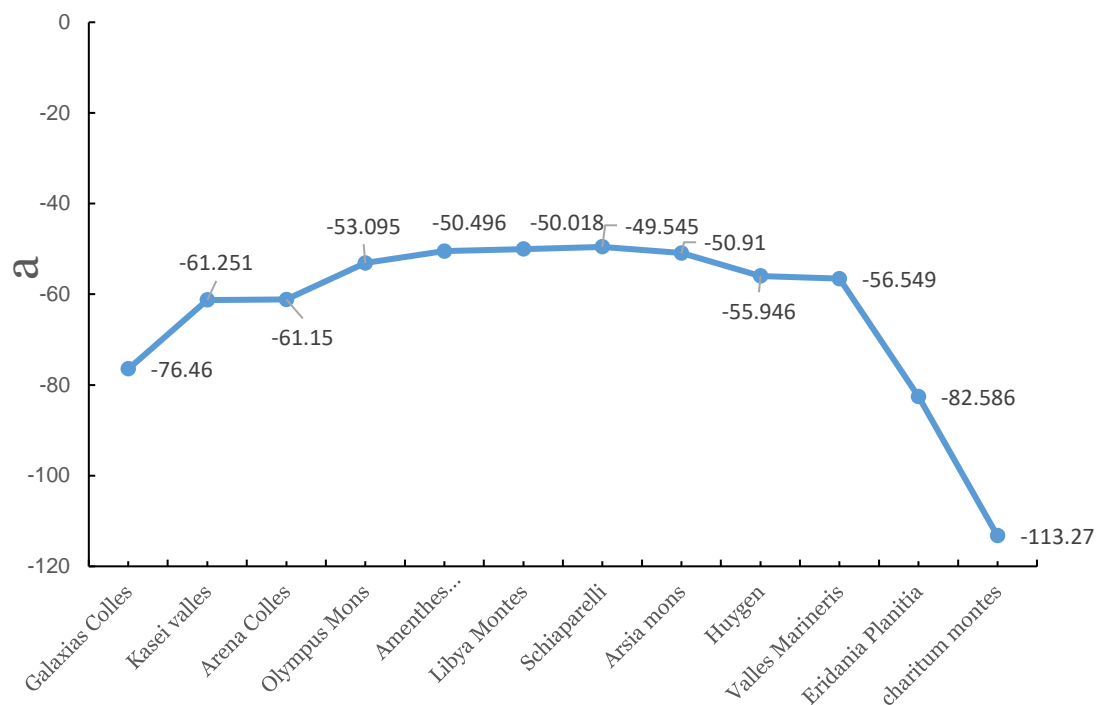


Figure 11. The descending rate of PSD affected by latitude. The sample areas in this figure are sorted by latitude from left to right (39.07° N– 0° – 58.1° S). The descending rate of SASR and PSD showed the same trend: from the northern hemisphere to the equator, the rate became slower; Then, from the equator to the southern hemisphere, the rate becomes faster.

3.2. Characteristics of Spectrums in Four Seasons

Since Martian moving orbits and velocity are different from Earth, the durations of Martian seasons are not evenly distributed. This paper divided four seasons of Mars according to Table 2 (employed in MCD). Then, we extracted S_sR and S_sP in four seasons respectively. The employed method was in common with the method used in the annual spectrum.

As seen in Figures 12 and 13, since the spectrums in four seasons represent stable spatial structures of SASR or PSD for four different seasons on Mars, the seasonal combination spectrum can be used to reveal the temporal distribution of spatial structure for SASR and PSD in different landforms under terrain relief. We used it to analyze the variation law of SASR and PSD in different sample areas under topographic relief.

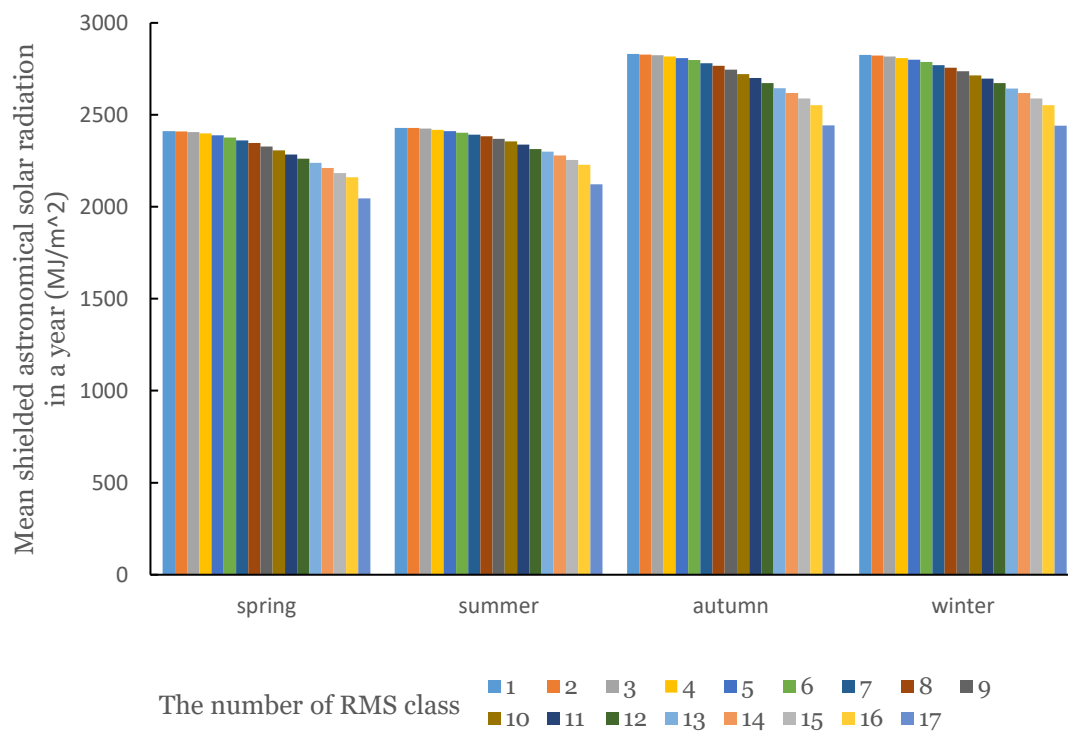


Figure 12. Roughness-mean shielded astronomical solar radiation spectrums of Valles Marineris in spring, summer, autumn, and winter. Due to the space limitation, the seasonal spectrum in other regions was not presented.

3.2.1. The Law of Gradual Variation of R_sS and R_sP with Terrain Relief in the Annual Spectrum

The spectral curve of S_sR and S_sP in each season generally showed a downward trend with the increase of the number of RMS classes in each season, which was similar to the annual spectrums (see Figures 12 and 13). The explanation for these characteristics may be consistent with the above explanation provided for the annual spectrums. That is, no matter the temporal scale, year or season, SASR and PSD keep a regular downward trend with the increase of terrain relief. We may infer that the rugged terrain generally obtained the weaker PSD and SASR due to the shielding effect caused by the more complex terrain.

3.2.2. Latitude Anisotropy Characteristics Influenced by the Shielding Effect in R_sS and R_sP

Furthermore, we found that with the latitude varying, characteristics discovered in the S_sR and S_sP between four seasons showed a certain of regularity. This finding will be of interest that the variation of SASR and PSD on Mars was different from that on Earth. Characteristics in PSD and SASR between four seasons for the same landforms respectively were discussed as follows.

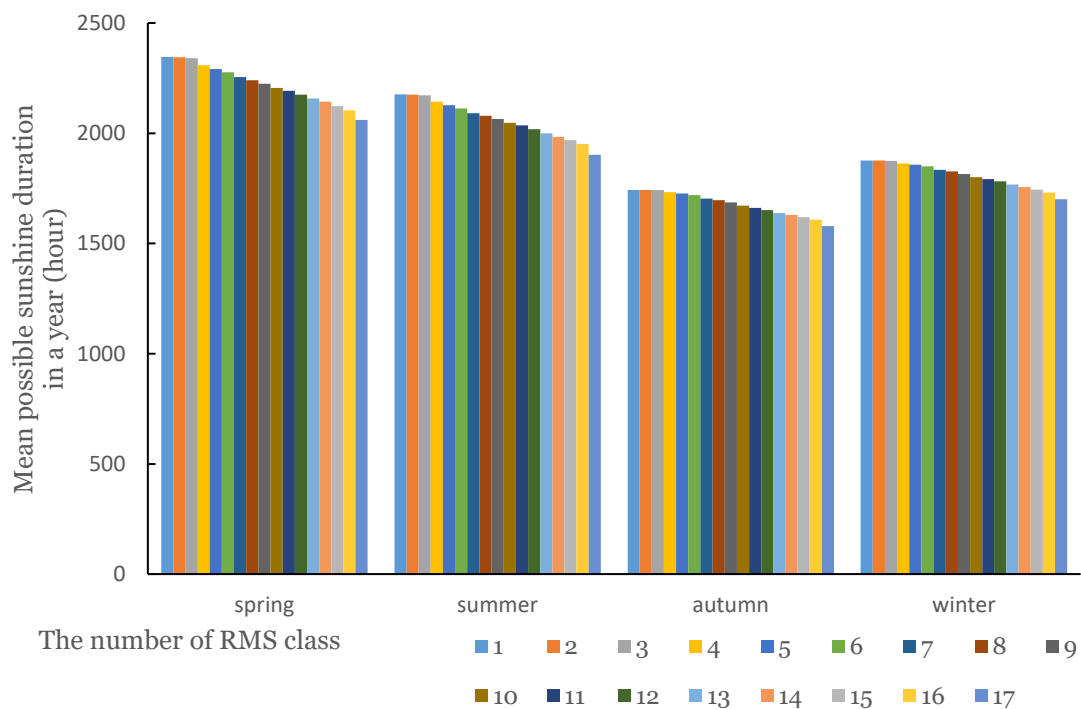


Figure 13. Roughness-mean possible sunshine duration spectrums of Valles Marineris in spring, summer, autumn, and winter.

PSD, in the sample area of the northern hemisphere, within each roughness class, all decreased in the following order: spring, summer, winter, autumn. This order was consistent with the order of Martian imbalanced ratio of four seasons (the ratio of the duration of each season). However, in the sample area of the southern hemisphere, PSD did not decrease in the same order even decreased in the disorder order (see Table 3). These characteristics were different from Earth. Theoretically, as discussed in result 2, the PSD for a day was determined by two factors: the PSD from sunrise to sunset determined by solar azimuth and the decreased PSD determined by solar elevation angle. Take the northern hemisphere on Earth as an example, since the sample area is in the northern hemisphere, the sun elevation angle is at its maximum in summer and at its minimum in winter, respectively. The sun elevation angle in spring and autumn lies between them. Besides, the sun elevation angle affects the intensity of the shielding effect (see Figure 8). The higher sun elevation angle may lead to the weaker shading effect, while the weaker shading effect causes the increase of the PSD. Meanwhile, as the sun is directly in the northern hemisphere in spring and summer, the solar azimuth may cause the total period of daytime (from sunset to sunrise) to increase, which may cause more light to be received in summer and spring. That is, the theoretical PSD without considering the shielding effect may bring certain influences to different seasons. Therefore, based on the abovementioned two reasons, the PSD in the northern hemisphere of the Earth generally decreased in the following order: summer, spring, autumn and winter, which was confirmed by [12]. Similarly, we can infer that PSD in the southern hemisphere of the Earth generally decreased in the following order: winter, autumn, spring and summer. However, according to the above, the seasonal characteristics of sample areas on Mars discovered in S_5P was different from Earth. Then, we aimed to explore the reasons before this phenomenon.

Table 3. Statistics of 6 sample areas and 2 test areas of the southern hemisphere.

| Sample Area | Center Latitude | Descending Order of Mean Maximum Daily PSD | Descending Order of Mean Daily Shielding Effect | Descending Order of Mean Daily PSD | Descending Order of Mean PSD | Descending Order of PSD (in S_2P within Each Roughness Class) | Descending Order of SASR (in S_1P within Each Roughness Class) |
|---------------------------|-----------------|--|---|------------------------------------|------------------------------|---|--|
| schiaparelli | −2.71° | C, D, A, B | B, A, C, D | B, A, D, C | A, B, D, C | A, B, D, C | C, D, B, A |
| Arsia mons | −8.61° | C, D, A, B | B, A, C, D | B, A, D, C | A, B, D, C | A, B, D, C | C, D, B, A |
| Huygens | −13.88° | C, D, A, B | B, A, C, D | C, D, A, B | A, B, D, C | A, B, D, C | C, D, B, A |
| Valles Marineris | −14.01° | C, D, A, B | B, A, C, D | C, D, A, B | A, B, D, C | A, B, D, C | C, D, B, A |
| North of the Hellas Plain | −34° | C, D, A, B | B, A, C, D | C, D, A, B | D, C, A, B | | C, D, B, A |
| Eridania Planitia | −38.15° | C, D, A, B | B, A, C, D | C, D, A, B | D, A, C, B | D, A, C, B | C, D, B, A |
| South of the Hellas Plain | −48.75° | C, D, A, B | B, A, C, D | C, D, A, B | D, C, A, B | | C, D, B, A |
| charitum montes | −58.1° | C, D, A, B | B, A, C, D | C, D, A, B | D, C, A, B | D, C, A, B | C, D, B, A |

We found the reason before this finding was mainly because of the imbalanced seasons caused by Martian moving orbits and velocity (see Table 1). This unique Martian movement causes the durations of spring and summer on Mars are much longer than autumn and winter (the ratio of durations for spring, summer, autumn and winter is: 1.34: 1.25:1: 1.08, while the Earth's is nearly 1:1:1:1). Then, this imbalanced duration of seasons resulted in the weakening influences of the total shielding effect to PSDs in each season. The descending order of PSDs in the sample area of the northern hemisphere, within each roughness classes, all decreased in the consistent order with the descending order of the duration of four Martian seasons (spring, summer, winter, autumn). In the southern hemisphere, the descending order of PSDs in the sample area at first affected by the unbalanced seasons still maintains the same descending order (spring, summer, winter, autumn). Then, affected by the maximum PSD in a day for each season and the shielding effect, the descending order of PSDs gradually varied. The conclusion can be verified by the following steps:

Step 1. We considered the duration of mean daily maximum PSD in each season. Two test areas were added to verify the characteristics in the southern hemisphere (the northern part and southern part of Hellas Plain). We calculated the theoretical maximum PSD in each season for these six regions and denoted as P_{\max} (added up the period from sunrise to sunset of every day in each season). Then, we divided P_{\max} in each season by its corresponding number of days to get the mean daily maximum PSDs (it is hereafter called P_{dmmax} for brevity). In the southern hemisphere, the P_{dmmax} in each season generally decreased in the following order: autumn, winter, spring, and summer; besides, as latitude increased, the influences of P_{dmmax} gradually enhanced and became the leading factor (the ratio of P_{dmmax} in four seasons ranged from 1.0002:1:1.0179:1.0177 to 1.0094:1:1.8944:1.8846). Regions in the southern hemisphere do not violate the rules mentioned above; when the sun is directly in the southern hemisphere, autumn, and winter have more daytime hours than spring and summer. It is the result of the influence of the solar azimuth.

Step 2. We considered the ratio of daily shielding effect (it may be called R_S for convenience) in each season. We calculated the actual daily PSD as P_a . The reduced PSD denoted as P_r in each season was the difference between the P_{\max} and P_a . Furthermore, the ratio of daily shielding effect in each season was viewed as the ratio of P_r to P_{\max} . Then, we calculated the ratio of the daily shielding effect in four seasons (see Table 3). The descending order of daily shielding effect ratio was generally in the following order: summer, spring, autumn, winter. Additionally, the R_S is generally less than 6%. Then, we may draw an inference: although the shielding effect has little influence on the descending order of daily PSD, the daily shielding effect has a consistent law which may lead to the same trend of seasonal PSD. It is the result of the influence of the sun elevation angle.

Step 3. Based on the above two experiments, we draw a more general conclusion: the daily PSD was influenced by theoretical daily maximum PSD and the daily shielding effect. Compared to the daily shielding effect, the theoretical daily maximum PSD was the leading factor. Along with the order of autumn, winter, spring, and summer, the mean theoretical daily maximum PSD decreases, the mean daily shielding effect leads to little influence. Then, influenced by these two determine factors, the PSD may decrease in the following trend: autumn, winter, spring, and summer. However, the imbalanced seasons impede the trend of PSD (This can be observed in Table 3, the original order of the seasons of landforms at low latitudes were the same as the order of unbalanced seasons. Then, with latitude increasing, the descending order of four seasons for corresponding landform gradually approached to the previously mentioned trend). It is the combination of these three factors that make the law of seasons different from the Earth.

Step 4. This stage was to prove the conclusions proposed in stage 3. We considered the performance of mean daily PSD in each season. We calculated the PSD of the sample regions in each season. Then, we divided the seasonal PSD of each season by its corresponding number of days to get the mean daily PSDs in each season. We found that the seasonal mean daily PSD was affected by the mean theoretical daily maximum PSD and the mean daily shielding effect. From the equator to the southern hemisphere, it quickly approached to

the descending trend mentioned in stage 3: autumn, winter, spring and summer. However, due to the imbalanced seasons, the seasonal PSD at the beginning did not decrease in the same order as the seasonal mean daily PSD. It decreased in the following order: spring, summer, winter and autumn, which was the same with the descending order of imbalanced seasons. Then, with latitude increasing, it gradually varied into the sequence: autumn, winter, summer and spring, which was influenced by the mean daily maximum PSD and the shielding effect. That is, obviously, it can be concluded that although the descending order of mean daily PSDs in each season was nearly consistent with the descending order of mean daily maximum PSDs, the imbalance of seasons weakens the influences on the total PSD in each season.

Step 5. We also calculated the mean daily maximum PSDs, shielding effect ratio, and mean daily PSD for all sample areas in the northern hemisphere in each season. With latitude increasing, the influences of P_{dmmax} gradually enhanced and became the leading factor (the ratio of P_{dmmax} in four seasons ranged from 1.0174: 1.0176: 1: 1.0002 to 1.3419: 1.3453: 1: 1.0036). The descending order of shielding effect ratio was autumn, winter, summer, and spring. Besides, the shielding effect ratio was generally less than 7%, which may lead to little influence on the descending order of total PSD in four seasons. Then, we found that under the influences of shielding effect and theoretical daily maximum PSDs, the descending order of mean daily PSDs was generally the same as theoretical daily maximum PSDs (that is, summer, spring, winter, autumn). However, due to the imbalanced Martian seasons, the descending order of PSDs in four seasons generally was: spring, summer, winter, autumn, which was in common with the descending order of imbalanced Martian seasons. That is, the inference we derived in the southern hemisphere was also confirmed in the northern hemisphere.

Note that we found that the descending order of the PSDs in S_sP in four Martian seasons within each roughness class showed the same trend with the actual descending order of seasonal mean PSD no matter in the northern hemisphere or southern hemisphere. That is, S_sP was able to reveal the relationship of PSD of four seasons in sample areas.

Besides, stage 2 and stage 5 provide deep support for the explanation for result 4. In the different sample areas of the northern hemisphere, along with the increase of latitude, the increase of PSD in spring and summer was generally greater than the decrease of PSD in autumn and winter. These findings lead to the result that the annual PSD decreased with latitude decreasing in the northern hemisphere.

Differently, the S_sR found by us in four seasons in the sample areas showed different characteristics with the S_sP . In the sample regions of the northern hemisphere, the S_sR in each roughness class generally decreased in the following order: summer, spring, autumn, and winter; in the sample region of the southern hemisphere, the S_sR decreased in the following order: autumn, winter, summer, and spring. Then, we considered the influences of the shielding effect and mean daily SASR in four seasons. In common with PSD, we calculated the theoretical maximum SASR as S_{max} (the SASR from sunrise to sunset, which did not consider the shielding effect) and the daily shielding effect ratio of SASR which was similar to the method in PSD. We found that the SASR among four seasons in the northern hemisphere displayed the same descending order as that of the mean daily PSD among for season.

The reason before the phenomena that the descending order of SASR in four seasons was consistent with that of mean daily SASR in four seasons may be explained as follows. The SASR was also affected by the imbalance of seasons. But this effect may be counteracted by the shielding effect and mean daily SASR in four seasons. On the one hand, the descending order of shielding effect ratio of SASR was consistent with that of PSD. On the other hand, in each sample area, the shielding effect ratio in each season of SASR was greater than the shielding effect ratio in each season of PSD (the former minus the latter is about 0.03-1.1%). Besides, huge differences were exit on the ratio of mean daily SASR in each season, which was different from PSD (in charitum montes, the ratio of SASR in four seasons can even reach 1:1.099:5.5739:5.1697, while the ratio of PSDs in four seasons were

1.0093:1:1.8943:1.8846). That is, different from PSD, the shielding effect and mean daily SASR in each season may obviously influence the total SASR in each season. Then, under the dual effects of these two factors, the effect of the imbalanced seasons on SASR may be nearly counteracted. This conclusion was confirmed by the fact that the SASR displayed an opposite descending order of the mean daily SASR.

We extracted the decay rate of S_sR and that of S_sP in four seasons (the similar experimental method in result 4) and found the features similar to annual spectrums: along with latitude decreasing, the decay rate gradually decreases (see Figures 14 and 15). It may be summarized that the attenuation rate gradually decreased from the sample areas of high latitudes in the northern hemisphere to the equator, and then gradually increased from the equator to the sample areas of high latitudes in the southern hemisphere. This feature may be explained by the similar ways we provided for the same features in the annual spectrum.

Note that we may obtain a more general conclusion: SASR is more sensitive to terrain influences than PSD. This was proved by the finding that the decay rate of SASR is generally greater than that of PSD (see Figures 16 and 17). Besides, the phenomenon that the shielding effect ratio in each season of SASR was greater than the shielding effect ratio in each season of PSD in the sample area also proved this conclusion. That is, the SASR may be highly influenced by the shielding effect than PSD.

In Table 3, A represents spring, B represents summer, C represents autumn, and D represents winter. As seen in this table, under the influence of solar azimuth, the mean maximum daily PSD decreased in the following order: C, D, A, B; under the influence of solar elevation angle, the shielding effect of PSD generally decreased in the following order: B, A, C, D. Then, these two factors may become the determine factors of mean actual daily PSD. Thus, the mean actual daily PSD quickly varied to the same descending order of mean maximum daily PSD. That is, the daily PSD on Mars showed enough regularity due to the influences of solar azimuth and solar elevation angle. However, due to the imbalanced period of seasons on Mars, the seasonal PSD does not go down in the same order as the mean actual daily PSD. The seasonal PSD at the beginning decreased in the same descending order of duration in each season: A, B, D, C (the period ratio of spring, summer, winter and autumn on Mars is 1.34: 1.25:1: 1.08). Then, with the increase of latitude, the influence of sun azimuth and sun elevation angle increased; then, it caused the descending order of PSD to gradually varied. It is a gradual process. Finally, it became a fixed order: D, C, A, B.

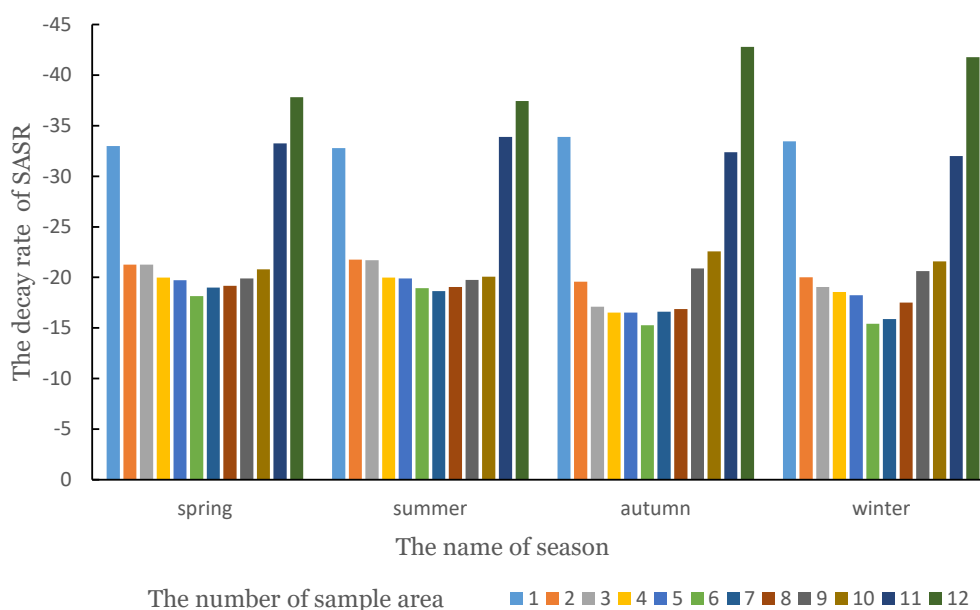


Figure 14. The decay rate of roughness-mean shielded astronomical solar radiation spectrums in four seasons in 12 sample areas.

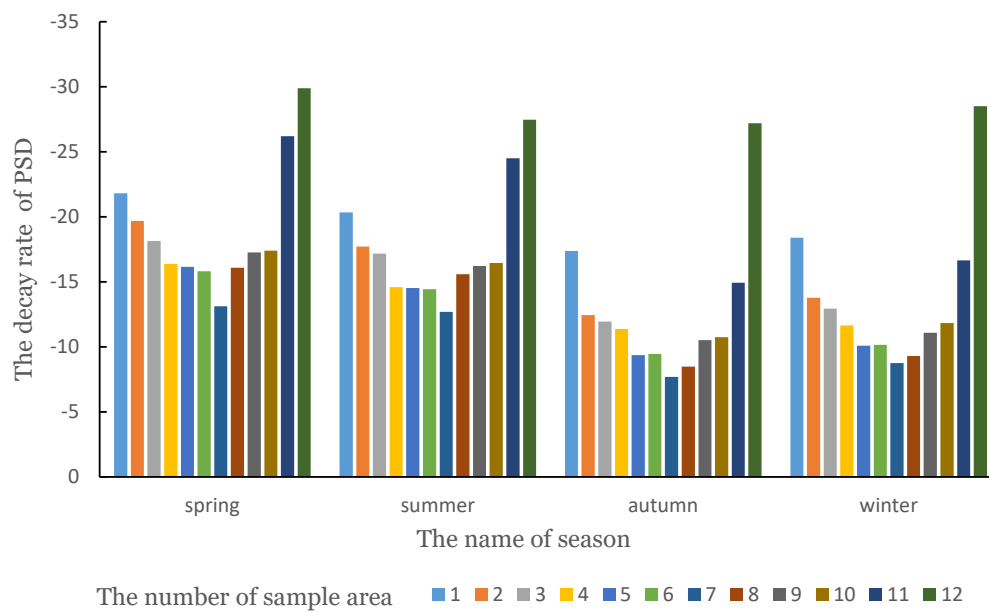


Figure 15. The decay rate of roughness-mean possible sunshine duration spectrums in four seasons in 12 sample areas.

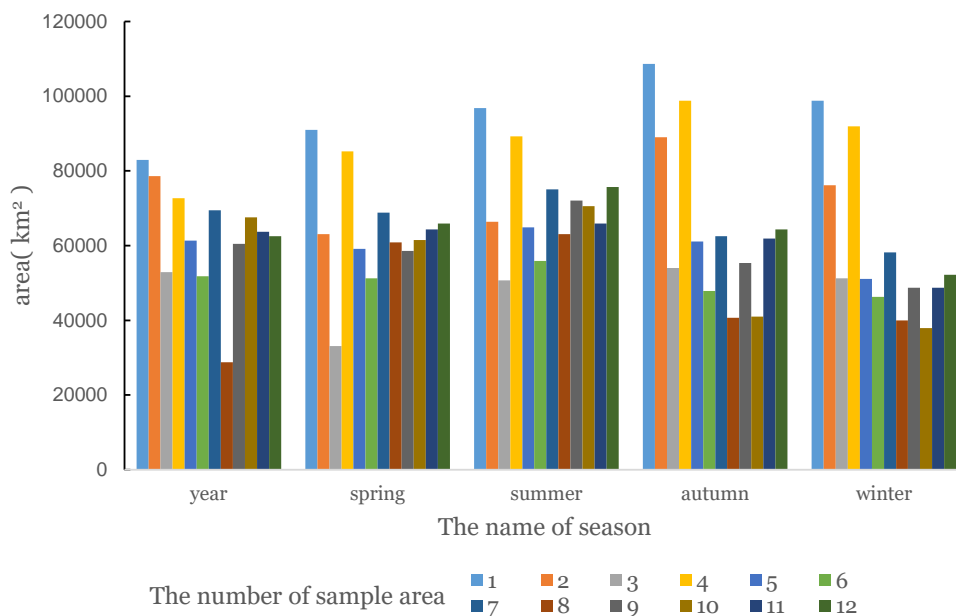


Figure 16. Values of critical areas for the roughness-mean possible sunshine duration spectrums in each season (denoted as X_2).

3.2.3. Relationship between Critical Areas for Spectrums in Four Seasons

Additionally, we discovered that increasing order of X_{2s} in four seasons was the same as the increasing order of shielding effect ratio (see Figure 16). The reasons before this characteristic may be explained as follow. The PSD in each season generally approached to the maximum PSD in four seasons (i.e., the period from sunrise to sunset in each season, which did not consider the shielding effect). On the other hand, there may be an ideal stable space structure for PSD when PSD was not affected by the shielding effect. The weaker the shielding effect, the closer the PSD is to the maximum PSD, the higher the similarity of PSD in the grid will be, and vice versa. Afterwards, under the above, if the shielding effect enhanced, the similarity of PSDs in the grids may weaken. A larger critical area is needed to guarantee the stable spatial structure of PSD. Accordingly, the closer the

PSD is to the maximum PSD, the smaller X_{2s} maybe. That is, the X_{2s} may decrease in the same order as the descending order of shielding effect.

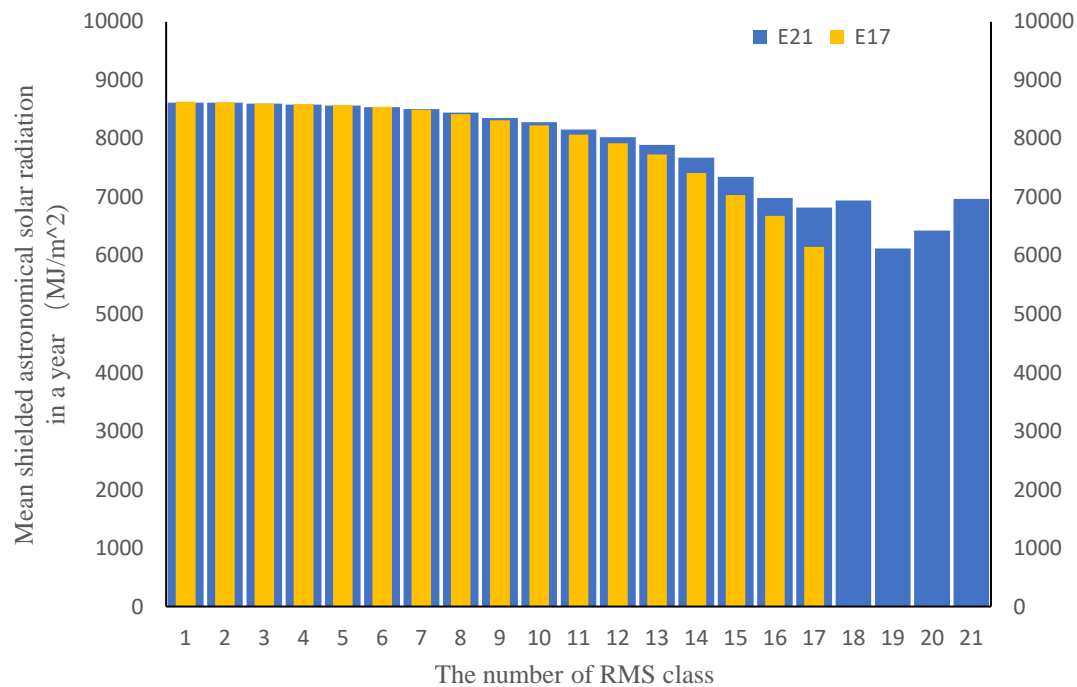


Figure 17. Roughness-mean shielded astronomical solar radiation spectrums of Valles Marineris based on E 9 and E 17 in a year. In E 17, an 5 m equal-interval roughness classification scheme is adopted (i.e., the roughness is classified into 17 classes: 0–5 m, 5–10 m, 5–10 m, 10–15 m, 15–20 m, 20–25 m, 25–30 m, 35–40 m, 40–45 m, 45–50 m, 50–55 m, 55–60 m, 60–65 m, 65–70 m, 70–75 m, 75–80 m, 80 m–). In E 21, an 10 m equal-interval roughness classification scheme is adopted (i.e., the roughness is classified into 28 classes: 0–5 m, 5–10 m, 5–10 m, 10–15 m, 15–20 m, 20–25 m, 25–30 m, 35–40 m, 40–45 m, 45–50 m, 50–55 m, 55–60 m, 60–65 m, 65–70 m, 70–75 m, 75–80 m, 80–85 m, 85–90 m, 90–95 m, 95–100 m, 100 m–). As presented in the figure, when the classified roughness is greater than 80 m (lie in the 18, 19, 20, 21 class), the spectrum showed a tendency to be unstable. This is mainly because when the critical region is expanding, few grids within the roughness class of 18–21 are obtained (as observed, only about 1–3 number of the corresponding grids in each class were obtained). These grids can be regarded as singular values and are not representativeness of statistical significance.

Furthermore, the annual PSD was yielded from summing the PSDs of four seasons. That is, the above characteristics may further result in a relationship between X_{2s} in year and X_{2s} in the four seasons. As seen in Figure 18, the X_{2s} in a year were generally between the maximum and minimum of X_{2s} in four seasons in each sample area. This finding may be similar explained by how a similar manner in which we explained the descending order of X_{2s} in the four seasons. It may be also a homogenized result of PSD in a year which generally approached to the maximum PSD in a year. However, due to the PSD in a year being a cumulative result of four PSDs of four seasons, the degree of homogenization of PSD in a year may between the maximum and minimum homogenization of PSD in four seasons.

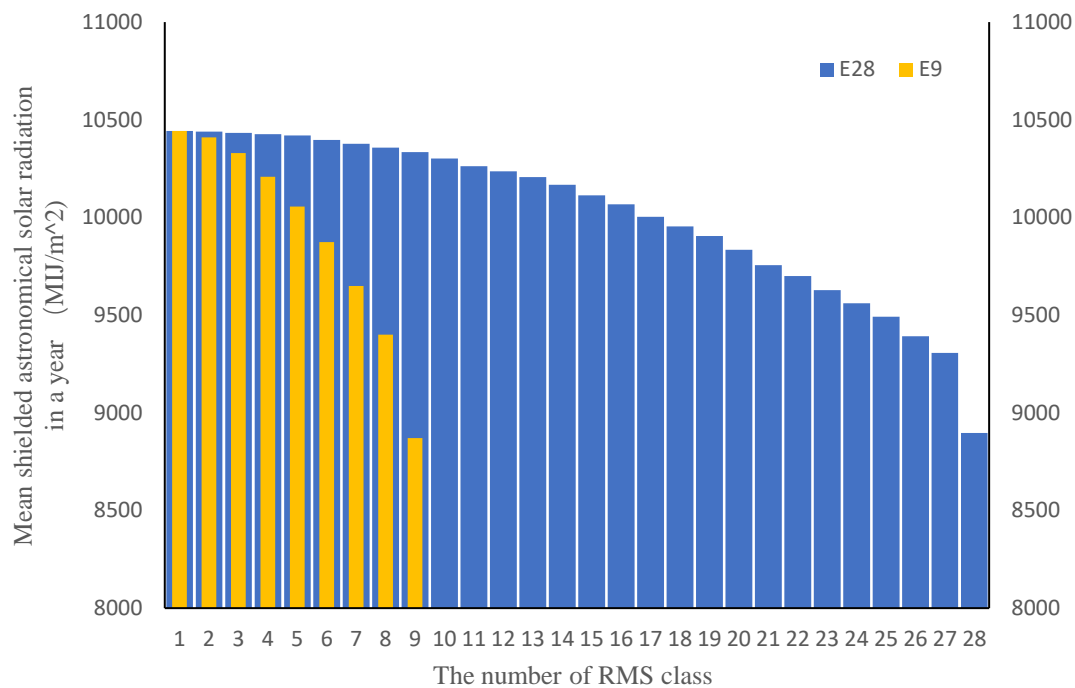


Figure 18. Roughness-mean shielded astronomical solar radiation spectrums of Valles Marineris based on E 9 in a year. In E 9, an 10 m equal-interval roughness classification scheme is adopted (i.e., the roughness is classified into 9 classes: 0–10 m, 10–20 m, 20–30 m, 30–40 m, 40–50 m, 50–60 m, 60–70 m, 70–80 m, 80 m–) In E 28, an 10 m equal-interval roughness classification scheme is adopted (i.e., the roughness is classified into 28 classes: 0–3 m, 3–6 m, 6–9 m, 9–12 m, 12–15 m, 15–18 m, 18–21 m, 21–24 m, 24–27 m, 27–30 m, 30–33 m, 33–36 m, 36–39 m, 39–42 m, 42–45 m, 45–48 m, 48–51 m, 51–54 m, 54–57 m, 57–60 m, 60–63 m, 63–66 m, 66–69 m, 69–72 m, 72–75 m, 75–78 m, 78–81 m, 81 m–).

Meanwhile, we also found the X_{1s} in four seasons in each sample area. The increasing order of X_{1s} in four seasons was also the same as the increasing order of shielding effect ratio. SASR was affected by the shielding effect and PSD. Then, the SASR may tend to the maximum SASR (i.e., the SASR from sunrise to sunset, regardless of shielding effect). That is, SASR may be homogenized. In common with PSD, we can infer that this homogenized characteristic may lead X_{1s} to increase in the same order of shielding effect. Then, we proved this explanation for this finding. We calculated the variation coefficient of SASRs in each season in each sample area. We found that the descending order of the variation coefficient of SASR in each sample area is the descending order of the shielding coefficient. That is, the larger the shielding coefficient, the more complex the distribution of SASR in the sample area. The complex distribution of SASR may lead to a larger X_{1s} .

Regardless of the year or season, the value of X_{1s} was generally greater than X_{2s} (the ratio of X_{1s} to X_{2s} ranged from 1.12 to 2.172). This finding can be explained as follows. Based on Equation (13), the PSD is a principal parameter of SASR which may greatly influence SASR. Besides, since there are other involved parameters in the calculation of SASR, (such as slope, aspect.), the distribution of SASR may be more complex than PSD. When we found the X_{2s} , due to the more complex SASR, a larger area may be required to obtain the similarities in the distribution of SASR. Accordingly, for the same duration (a year or each season), X_{1s} may be generally greater than X_{2s} .

Furthermore, in common with X_{2s} , the X_{1s} in a year was between the maximum and minimum of X_{1s} in four seasons. The reason behind this characteristic of X_{1s} may be explained in the same way we explained the reason for the similar characteristic in X_{2s} . These findings were confirmed by the following Equation:

$$X_{2s\text{-year}} = (X_{2s\text{-spring}} + X_{2s\text{-summer}} + X_{2s\text{-autumn}} + X_{2s\text{-winter}}) / 4 \quad R^2 = 0.74 \quad (41)$$

$$X_{1s-year} = (X_{1s-spring} + X_{1s-summer} + X_{1s-autumn} + X_{1s-winter}) / 4 \quad R^2 = 0.79 \quad (42)$$

4. Discussion

Combining planetology, Martian solar radiation theory, and the astronomical radiation theory on Earth, a complete process to calculate the Martian SASR and PSD was proposed in this paper. Compared to the previous research on Mars, this method took the terrain influences into account for the first time. That is, to some extent, it improved the accuracy of the previous models. Thus, this method is promising for future works about SASR on Mars. The spectrum using the slope as the x-axis was not suitable to be adopted on Mars. Thus, this paper proposed the new concept of spectrums for PSD and SASR, which was tested to be suitable for the study of SASR and PSD on Mars. The parameter to describe terrain relief is roughness. The RMS, which was generally viewed as a terrain parameter to describe roughness, was adopted to reveal the roughness on the Martian surface. However, although RMS was adopted as a terrain parameter in common with the slope to describe planetary surface topographic relief, it has never been used in spectral studies. According to the finding of the result, it is clear that S_sR and S_sP can be efficient in exploring the special spatial-temporal distribution of SASR and PSD. The discussion about findings was as following respects:

(1) SASR and PSD showed the law of gradual variation with terrain relief. Either on an annual scale or a quarterly scale, the value of S_sR and S_sP in different Martian landforms generally decreased. This phenomenon may reveal that SASR and PSD were highly influenced by terrain relief. In each sample area, the rugged terrain may cause the decrease in SASR and PSD. S_sR and S_sP in a year or four seasons revealed the interaction of SASR and PSD with terrain relief.

(2) Under the influences of shielding effect, the seasonal and annual spatial structure of SASR or PSD on Mars revealed by S_sR and S_sP showed the latitude anisotropy characteristics. The descending order of S_sR and S_sP in four seasons showed a certain regularity: the attenuation rate decreased from the sample areas of high latitudes in the northern hemisphere to the equator, and then increased from the equator to the sample areas of high latitudes in the southern hemisphere. This regularity is affected by the sun elevation angle and sun azimuth, which are further affected by the shielding effect. That is, it is still a manifestation of the terrain influences on SASR and PSD.

(4) As discussed in the results, according to the findings of S_sR and S_sP , the law of the SASR and the PSD on Mars varied with latitude are totally different from those on Earth, either on an annual scale or on a quarterly scale. This was mainly because of the imbalanced seasons of Mars. Besides, SASR is more regular than PSD. The reason before this feature may be because SASR is more sensitive to the shielding effect than PSD. In all sample areas, the finding that attenuation rate of S_sR was greater than S_sP and the finding that the shielding effect ratio of SASR was greater than PSD provided deep support for this explanation.

(5) The X_{1s} and X_{2s} are effective indexes to reflect the stable spatial structure of SASR and PSD respectively in different geomorphology. The X_{1s} and X_{2s} may be regarded as minimum test areas in this sample area for the research on SASR or PSD since it showed sufficient stability when the test area is larger than those. Besides, the X_{1s} and X_{2s} in a year seemed to be positively correlated with the variable coefficients of roughness. And the X_{1s} and X_{2s} in a year may be the mean of that in four seasons. The increasing order of X_{1s} and X_{2s} in four seasons was the same as the increasing order of shielding effect ratio. These relations may help us quickly determine the minimum test area of the sample area.

Note that the terrain analysis on Mars provides additional insights beyond planetary, astronomical and climatological parameters (which are not within the scope of this issue).

4.1. Discussion on the Influence of Roughness Classification Scheme on the Spectrum

The previous studies about spectrum slope classification scheme generally based on the following two points: in the spectrums proposed by previous studies, equal-interval

slope classification was generally used as a classification scheme better than other schemes to ensure that comparative studies can be conducted in each landform; besides, 45–90° were generally viewed as a single class since the grids with the value of slope between 45–90° accounts for little of the total grid area [11,12,78,79,133].

Referring to the above spectral design, we calculated the roughness of 50 randomly selected test areas and 12 sample areas on Mars and found the number of grids with the value of RMS greater than 80 m accounted for less than 6% of all grids (ranged from 0% to <5.83%) in any test area and sample area. Thus, for the roughness spectrum, we design the structure of roughness classification as a 5 m equal-interval roughness classification scheme: 0–5 m, 5–10 m, 10–15 m, 15–20 m, 20–25 m, 25–30 m, 30–35 m, 35–40 m, 40–45 m, 45–50 m, 50–55 m, 55–60 m, 60–65 m, 65–70 m, 70–75 m, 75–80 m, 80 m–(referring to the spectrums whose x-axis was slope, since the number of grids whose RMS value was greater than 80 m accounted for less than 6% of all grids in any sample area, RMS whose value was greater than 80 m was used as a single class in the spectral scheme). We also seek to further classify the grids whose RMS is greater than 80 m. It was not able to be extracted in some regions of flat terrain such as impact craters or planitia (because there are no grids whose RMS was greater than 80 m) or display the disorder trend for different S_sR and S_sP in the class whose RMS value was greater than 80 m (see Figure 17).

We discovered the corresponding S_sR and S_sP in each sample area by adopting the 5 m equal-interval roughness classification scheme (called E 17 for convenience, see Figure 17). Then we seek to explore different influences of different roughness classification on the spectrums. we also investigated the corresponding $S_{1s}P$ and $S_{2s}P$ in each sample area by adopting the 3 m equal-interval roughness classification scheme (called R 28 for convenience, see Figure 18) and 10 m equal-interval roughness classification scheme (called E 9 for convenience, see Figure 18).

The corresponding characteristics in E 17 can be also found in the E 28 and E 9: e.g., along with the roughness class increasing, the corresponding S_sR and S_sP in a year and in four seasons generally decreased. The relationship of S_sR and S_sP in sample area in four seasons based on E 24 and E 9 were also consistent with the law of E 17. The explanation for this result can be in the same way as E 17.

The same spectral characteristics found on the corresponding spectrums based on different equal-interval roughness classification reveals the reliability of the characteristics in SASR and PSD which we found on Mars. In other words, it seems that the spectrum methods proposed by us show a certain remarkable ability in accurately revealing the spatial-temporal distribution characteristics of SASR and PSD.

4.2. The Commonalities and Differences between the Two Spectrums and Other Spectrums Proposed Before

We discussed the commonalities and differences of the proposed spectrum method and other spectrums before as follows.

4.2.1. Commonalities

(1) In Characteristics

The S_sR , S_sP , slope-mean SASR spectrum and slope-PSD ratio spectrum [11,12] originated in slope spectrum [77,78].

The spectrum method generally adopted a form of two-dimensional spectrum to reveal the stable spatial structure of specific matter composition (slope, PSD or SASR). Namely, they usually performed as a group of the histogram.

The morphology of previous spectrum method, S_sR and S_sP is closely related to the extracted region. For each style of spectrum, the critical area generally exists in different landforms. Each spectrum can only be found when the extracted region was larger than the critical area. Besides, when the extracted region was larger than the critical area, the spectrums extracted in any location of sample area generally present self-similarity and stability.

Furthermore, the slope spectrum is the theory of geomorphological principles, which is employed to discover the stable structure of slope. The innovation of the other derivative spectrums is the application of geomorphological principles to astronomy, which were proposed to explore the stable spatial structure of SASR or PSD.

(2) In Findings

The spectrums may be viewed as the representative features of different landforms either on Mars or Earth. The spectrum method was successfully employed to explore the stable spatial structure of SASR or PSD in different landforms. The revealed stable structure of different landforms was generally closely related to its topography.

The spectrums revealed the temporal distributions of SASR or PSD for the corresponding landform. For each landform, as observed in the spectrums, the spatial structure of SASR or PSD in different temporal scale is different.

In the spectrums either on Mars or Earth, the SASR or PSD generally showed a downward trend in the corresponding spatial structure which revealed the interaction of SASR or PSD with terrain influences.

Besides, the SASR and PSD revealed by the spectrums generally showed a highly correlations with the shielding effect caused by the rugged terrain in different landforms.

The critical area of the spectrums seemed to be positively correlated to terrain complexity. Furthermore, certain relations seemed to be found between the critical areas of different temporal scale.

4.2.2. Differences

(1) In Characteristics

The application scope is different. The other spectrums cannot be found on Mars. The S_sR and S_sP was firstly proposed to be employed in the medium resolution DEM data for conducting the terrain analysis, which is convenient for the SASR and PSD study in Mars. The other spectrum was used to be employed in the high-resolution DEM data in Earth, which is not suitable for Mars.

The employed methods and application aim of the spectrums is different. The slope spectrum is the theory of geomorphological principles, which is employed to discover the stable spatial structure of the slope. The other spectrum originated from slope spectrum to explore the SASR or PSD. The slope-mean SASR spectrum and slope-mean PSD ratio spectrum adopted slope to explore the stable spatial structure of SASR or PSD shielding effect under terrain relief. According to the current situation of Martian study, the S_sR and S_sP were innovatively proposed to use roughness to describe the spatial structure of SASR and PSD under terrain relief. The RMS, which was generally regarded as a terrain parameter to describe roughness, was adopted to reveal the roughness on Martian surface. However, although RMS was usually adopted as a terrain parameter in common with slope to describe topographic relief, it has never been used in spectral studies.

Thus, the composition of the spectrum is different. Slope spectrum performed as a group of the histogram, whose x-axis is slope, y-axis is slope percentage. Slope-mean SASR spectrum performed as a group of the histogram, whose x-axis is slope, y-axis is mean SASR; slope-mean PSD ratio spectrum is a group of the histogram whose x-axis is slope, y-axis is the ratio of the mean PSD considering terrain influences on the mean PSD on the horizontal plane; S_sR and S_sP performed as a group of the histogram, whose x-axis is RMS, y-axis is mean SASR or PSD.

(2) In Findings

The spatial-temporal variations and laws of Mar revealed by spectrums was generally more complicated than Earth.

Different from the features of SASR and PSD on Earth revealed by [11,12], the SASR and PSD on Mars showed the unregular latitude anisotropy characteristics found in part 3. The descending order of SASR and PSD in four seasons was also different form Earth. As

discussed in the finding of part 3, the regularity is mainly because the imbalanced seasons caused by the differences of velocity and rotations between Mars and Earth.

In Mars, the spatial structure of SASR seemed to be more sensitive to the shielding effect than PSD unlike Earth, which is proven by our result.

The critical area of SASR and PSD was generally greater than that of [11,12]. The main reason for this is the total area of Martian landforms is generally larger than that of Earth.

The previous spectrums which based on slope area generally unable to be extracted on Mars. The spectrums based on RMS is suitable for Mars.

4.3. Limitations

The landform which has too flat terrain may lead to the failure of spectral extraction. We failed to extract the spectrum of dune fields though we have tried all approval dune fields (Abalos Undae, Aspledon Undae, Hyperboreae Undae, Ogygis Undae, Olympia Undae, Siton Undae). The mean value of the roughness for grids was less than 5 m. The percentages of the part of the area with roughness within the interval of 75–80 were between the value of 0 and 0.0015% and that of larger than 80 m were between the value of 0 and 0.00145%. Besides, the percentages of the part of the area with roughness larger than 30 m were less than 0.003% in the six dune fields. Obviously, the dune fields generally have a flat terrain. Then, we found that the roughness classes of the area which account for low percentages were failed to derive the corresponding value. Namely, when the topographic feature information of the landform is too little, we cannot derive the corresponding spectrums. On the other hand, it reflects the close relationship between the spectrum and the geomorphology.

4.4. Application of this Study

The models of SASR on Mars proposed in this paper can be used for future studies of astronomical radiation on Mars. Previous methods focus on the impact of the Martian meteorological environment on astronomical radiation but ignored the consideration of the terrain influence. This paper took the terrain influence into consideration, which is applicable for future research on Mars.

X_{1s} and X_{2s} may help researchers to determine the minimum test region of the sample areas. The spatial structure of SASR and PSD are stable only when the extracted region of the sample area is larger than the corresponding spectral critical area. Thus, they may be able to be as minimum test areas for corresponding research on SASR and PSD. If the extracted regions used to study SASR and PSD are less than the corresponding X_{1s} and X_{2s} , the obtained spatial structure of SASR and PSD may not reflect the distribution characteristics of those in this area. Moreover, in the 12 sample areas, sufficient positive correlation generally exists between X_{1s} and X_{2s} in a year and terrain relief (see Section 3.1). Thus, when we conducted research on the spatial distribution of SASR or PSD in a year, using the Equations proposed in 3.1 and the variable coefficient of roughness, we may be able to obtain minimum test regions for sample areas without the complex calculation process of obtaining the X_{1s} and X_{2s} . S_sR and S_sP , developed from the spectrum method in geoscience, were appropriate methods to reveal the spatial-temporal distribution of SASR and PSD on Mars. Different from the statistic method and the comparative method, S_sR and S_sP can reveal the complicated interaction between terrain relief and SASR or PSD. S_sR and S_sP in different areas generally showed different features, i.e., they respectively were able to reveal the differences of SASR or PSD between different regions under terrain relief.

The value of SASR in S_sR in each RMS class is the characteristic of the stable spatial structure of the corresponding sample area. That is, it can be regarded as the SASR's characteristic value in each RMS class of the corresponding sample area. Similarly, the value of PSD in S_sP in each RMS class can be regarded as the PSD's characteristic value in each RMS class of the corresponding sample area. Through the combination of roughness and S_sR and S_sP , we can quickly obtain the corresponding value of SASR and PSD in the sample area. The value of astronomical radiation and possible sunshine duration in a year

or four seasons may be quickly calculated by S_sR and S_sP proposed by us. The calculations for astronomical radiation and possible sunshine duration were so complex that it often requires the application of computer parallels to improve efficiency.

5. Conclusions

The models of SASR and PSD that can be applied to Mars are proposed. They compensate for the shortcomings of SASR and PSD models in previous Martian studies, taking into account terrain influences and improving time accuracy. These models can further extend to other Martian solar radiation models.

Different from the previous traditional geographic method such as the statistic method and comparative method, an innovative spectral method was proposed and applied to the study of SASR and PSD. We conducted experiments to extract the S_sR and S_sP of 12 Martian landforms. Then, we draw the following conclusions:

- (1) The spectral method is a quantitative method to be more effective in identifying and characterizing the spatial-temporal distribution of SASR or PSD in sample areas. The seasonal combination spectrum in four seasons is an effective qualitative description of the temporal distribution of SASR and PSD in different landforms.
- (2) S_sR and S_sP revealed the complex interactions between the SASR or PSD and the terrain relief. Under the terrain influences, in the S_sR and S_sP of the same landforms, the SASR and PSD showed a downward trend. This feature revealed that the SASR and PSD tended to decay under the influences of shielding effect caused by terrain relief.
- (3) SASR and PSD showed the latitude anisotropy characteristics. The latitude anisotropy characteristics discovered on Mars were complex and different from Earth due to the imbalanced seasons. In essence, this feature is also a manifestation of different shading effects caused by solar elevation angle.
- (4) SASR is more sensitive to the shielding effect than PSD which is proved by the corresponding experiments. Based on it, SASR showed more regular laws than PSD under terrain relief in a year or four seasons.
- (5) X_{1s} or X_{2s} can be a parameter to determine the minimum test regions for SASR or PSD of sample areas. The spatial structure of SASR or PSD become stable if the extracted region was larger than X_{1s} or X_{2s} . The relations discovered in results may help us to quickly found and test them.

Since the slope may be not appropriate to reveal the terrain relief on Mars, the method to extract X_{1s} and X_{2s} adopted roughness to successfully reveal the relations between terrain relief and SASR or PSD. This new spectral method theory sheds new light on the spatial-temporal structure of SASR and PSD and may provide a reference for the further future work of SASR and PSD on Mars.

The corresponding experiment result herein may prove that this method may be beneficial for us to explore the spatial-temporal distribution of SASR and PSD in different landforms on Mars. This method lays the groundwork and can be further extended to the study of the spatial-temporal structure of other solar radiation types.

The application of spectral method in this paper expands the application fields and techniques of spectral method. Additionally, our work advances the modeling and theoretical analysis of the solar radiation of Mars. It makes up for the deficiencies in the current relevant models and analyses.

Author Contributions: Conceptualization, Siwei Lin and Nan Chen; methodology, Siwei Lin and Nan Chen; software, Siwei Lin; validation, Siwei Lin and Nan Chen; formal analysis, Siwei Lin; investigation, Siwei Lin and Nan Chen; resources, Siwei Lin and Nan Chen; data curation, Siwei Lin and Nan Chen; writing—original draft preparation, Siwei Lin and Nan Chen; writing—review and editing, Siwei Lin and Nan Chen; visualization, Siwei Lin and Nan Chen; supervision, Nan Chen; project administration, Nan Chen; funding acquisition, Nan Chen. All authors have read and agreed to the published version of the manuscript.

Funding: This work was supported by the National Natural Science Foundation of China (grant numbers 41771423, 41491339, 41930102, and 41601408) and by the industry-university-research cooperation project for the social development of Fujian Province, China (grant number 2018Y0054).

Data Availability Statement: The data can be can be downloaded from the website: https://astrogeology.usgs.gov/search/map/Mars/Topography/HRSC_MOLA_Blend/Mars_HRSC_MOLA_BlendDEM_Global_200mp_v2.

Acknowledgments: The author would be heartfelt grateful to the anonymous reviewers' the helpful comments; the author also expressed his heartfelt thanks to his teacher Chen's guidance.

Conflicts of Interest: The authors declare no conflict of interest.

References

1. Landis, G.A. Solar radiation on mars—Stationary photovoltaic array. *J. Propuls. Power* **1995**, *11*, 554–561. [[CrossRef](#)]
2. Appelbaum, J.; Landis, G.A.; Sherman, I. Solar radiation on Mars—Update 1991. *Sol. Energy* **1993**, *50*, 35–51. [[CrossRef](#)]
3. Appelbaum, J.; Flood, D.J. Solar radiation on Mars. *Sol. Energy* **1990**, *45*, 353–363. [[CrossRef](#)]
4. Savijärvi, H.; Crisp, D.; Harri, A.M. Effects of CO₂ and dust on present-day solar radiation and climate on Mars. *Q. J. R. Meteorol. Soc.* **2005**, *131*, 2907–2922. [[CrossRef](#)]
5. Monteith, J.L. Solar Radiation and Productivity in Tropical Ecosystems. *J. Appl. Ecol.* **1972**, *9*, 747–766. [[CrossRef](#)]
6. Qiu, X.-F.; Zeng, Y.; Liu, S.-M. Distributed Modeling of Extraterrestrial Solar Radiation over Rugged Terrain. *Chin. J. Geophys.* **2005**, *48*, 1100–1107. [[CrossRef](#)]
7. Whiteman, C.D.; Allwine, K.J.J.E.S. Extraterrestrial solar radiation on inclined surfaces. *Environ. Softw.* **1986**, *1*, 164–174. [[CrossRef](#)]
8. Zeng, Y.; Qiu, X.; Miao, Q.; Liu, C. Distribution of possible sunshine durations over rugged terrains of China. *Prog. Nat. Sci.* **2003**, *13*, 761–764. [[CrossRef](#)]
9. Vicente-Retortillo, Á.; Valero, F.; Vázquez, L.; Martínez, G.M. A model to calculate solar radiation fluxes on the Martian surface. *J. Space Weather Space Clim.* **2015**, *5*. [[CrossRef](#)]
10. Khatib, T.; Abunajeeb, I.; Heneni, Z. Determination of Mars Solar-Belt by Modeling of Solar Radiation Using Artificial Neural Networks. *J. Sol. Energy Eng.* **2019**, *142*, 142. [[CrossRef](#)]
11. Chen, N. Spectra method for revealing relations between slope and possible sunshine duration in China. *Earth Sci. Inform.* **2020**, *13*, 695–707. [[CrossRef](#)]
12. Chen, N. Deriving the slope-mean shielded astronomical solar radiation spectrum and slope-mean possible sunshine duration spectrum over the Loess Plateau. *J. Mt. Sci.* **2020**, *17*, 133–146. [[CrossRef](#)]
13. Marzo, A.; Trigo-Gonzalez, M.; Alonso-Montesinos, J.; Martínez-Durbán, M.; López, G.; Ferrada, P.; Fuentealba, E.; Cortés, M.; Batlles, F.J.R.E. Daily global solar radiation estimation in desert areas using daily extreme temperatures and extraterrestrial radiation. *Renew. Energy* **2017**, *113*, 303–311. [[CrossRef](#)]
14. Ambreen, R.; Ahmad, I.; Qiu, X.; Li, M. Regional and Monthly Assessment of Extraterrestrial Solar Radiations in Pakistan. *J. Geogr. Inf. Syst.* **2015**, *7*, 58–64. [[CrossRef](#)]
15. Ambreen, R.; Ahmad, I.; Qiu, X.; Li, M. Regional and Monthly Assessment of Possible Sunshine Duration in Pakistan: A Geographical Approach. *J. Geogr. Inf. Syst.* **2015**, *7*, 65–70. [[CrossRef](#)]
16. Ahmad, M.J.; Tiwari, G.N. Solar radiation models—A review. *Int. J. Energy Res.* **2011**, *35*, 271–290. [[CrossRef](#)]
17. Zeng, Y. Distributed modeling of direct solar radiation on rugged terrain of the Yellow River Basin. *J. Geogr. Sci.* **2005**, *15*, 439. [[CrossRef](#)]
18. Sabo, L.M.; Mariun, N.; Hizam, H.; Radzi, M.A.M.; Zakaria, A. Estimation of solar radiation from digital elevation model in area of rough topography. *World J. Eng.* **2016**, *13*, 453–460. [[CrossRef](#)]
19. Reuter, H.I.; Kersebaum, K.C.; Wendroth, O. Modelling of solar radiation influenced by topographic shading—evaluation and application for precision farming. *Phys. Chem. Earth Parts A/B/C* **2005**, *30*, 143–149. [[CrossRef](#)]
20. He, Y.; Wang, K.; Zhou, C.; Wild, M. A Revisit of Global Dimming and Brightening Based on the Sunshine Duration. *Geophys. Res. Lett.* **2018**, *45*, 4281–4289. [[CrossRef](#)]
21. Bazrafshan, J.; Heidari, N.; Moradi, I.; Aghashariatmadary, Z. Simultaneous stochastic simulation of monthly mean daily global solar radiation and sunshine duration hours using copulas. *J. Hydrol. Eng.* **2015**, *20*, 04014061. [[CrossRef](#)]
22. Keating, K.A.; Gogan, P.J.; Vore, J.M.; Irby, L.R. A simple solar radiation index for wildlife habitat studies. *J. Wildl. Manag.* **2007**, *71*, 1344–1348. [[CrossRef](#)]
23. Hanqun, S.; Baopu, F.J.A.G.S. The elliptical integral model of computing the extraterrestrial solar radiation on the slope. *Acta Geogr. Sin.* **1996**, *6*, 559–566.
24. Chen, N. Scale problem: Influence of grid spacing of digital elevation model on computed slope and shielded extra-terrestrial solar radiation. *Front. Earth Sci.* **2020**, *14*, 171–187. [[CrossRef](#)]

25. Appelbaum, J.; Segalov, T.; Jenkins, P.P.; Landis, G.A.; Baraona, C.R. Verification of Mars Solar Radiation Model Based on Mars Pathfinder Data. In Proceedings of the Conference Record of the Twenty Sixth IEEE Photovoltaic Specialists Conference—1997, Anaheim, CA, USA, 29 September–3 October 1997; pp. 1039–1041. [\[CrossRef\]](#)
26. Appelbaum, J.; Steiner, A.; Landis, G.A.; Baraona, C.R.; Segalov, T. Spectral content of solar radiation on Martian surface based on Mars pathfinder. *J. Propuls. Power* **2001**, *17*, 508–516. [\[CrossRef\]](#)
27. Badescu, V. Available solar energy and weather forecasting on mars surface. *Mars Prospect. Energy Mater. Resour.* **2009**, *1*, 25–66. [\[CrossRef\]](#)
28. Badescu, V. Regional and seasonal limitations for Mars intrinsic ecopoiesis. *Acta Astronaut.* **2005**, *56*, 670–680. [\[CrossRef\]](#)
29. Badescu, V. Simulation of solar cells utilization on the surface of mars. *Acta Astronaut.* **1998**, *43*, 443–453. [\[CrossRef\]](#)
30. Badescu, V. Different strategies for maximum solar radiation collection on mars surface. *Acta Astronaut.* **1998**, *43*, 409–421. [\[CrossRef\]](#)
31. Cockell, C.S.; Raven, J.A. Zones of photosynthetic potential on Mars and the early Earth. *Icarus* **2004**, *169*, 300–310. [\[CrossRef\]](#)
32. Ghosh, H.R.; Bhowmik, N.C.; Hussain, M. Determining seasonal optimum tilt angles, solar radiations on variously oriented, single and double axis tracking surfaces at Dhaka. *Renew. Energy* **2010**, *35*, 1292–1297. [\[CrossRef\]](#)
33. Kuhn, W.R.; Atreya, S.K. Solar radiation incident on the Martian surface. *J. Mol. Evol.* **1979**, *14*, 57–64. [\[CrossRef\]](#) [\[PubMed\]](#)
34. Landis, G.A. Solar cell selection for Mars. *IEEE Aerosp. Electron. Syst. Mag.* **2000**, *15*, 17–21. [\[CrossRef\]](#)
35. Levine, J.S.; Kraemer, D.R.; Kuhn, W.R. Solar radiation incident on Mars and the outer planets: Latitudinal, seasonal, and atmospheric effects. *Icarus* **1977**, *31*, 136–145. [\[CrossRef\]](#)
36. Patel, M.R.; Zarnecki, J.C.; Catling, D.C. Ultraviolet radiation on the surface of Mars and the Beagle 2 UV sensor. *Planet. Space Sci.* **2002**, *50*, 915–927. [\[CrossRef\]](#)
37. Thiemann, E.M.B.; Chamberlin, P.C.; Eparvier, F.G.; Templeman, B.; Woods, T.N.; Bougher, S.W.; Jakosky, B.M. The MAVEN EUVM model of solar spectral irradiance variability at Mars: Algorithms and results. *J. Geophys. Res. Space Phys.* **2017**, *122*, 2748–2767. [\[CrossRef\]](#)
38. Vicente-Retortillo, Á.; Lemmon, M.T.; Martínez, G.M.; Valero, F.; Vázquez, L.; Martín, M.L. Variabilidad estacional e interanual de la radiación solar en las coordenadas de aterrizaje de Spirit, Opportunity y Curiosity. *Física Tierra* **2016**, *28*, 111–127. [\[CrossRef\]](#)
39. Zeitlin, C.; Hassler, D.M.; Guo, J.; Ehresmann, B.; Wimmer-Schweingruber, R.F.; Rafkin, S.C.R.; von Forstner, J.L.F.; Lohf, H.; Berger, T.; Matthiae, D.; et al. Analysis of the Radiation Hazard Observed by RAD on the Surface of Mars During the September 2017 Solar Particle Event. *Geophys. Res. Lett.* **2018**, *45*, 5845–5851. [\[CrossRef\]](#)
40. Badescu, V.; Popescu, G.; Feidt, M. Model of optimized solar heat engine operating on Mars. *Energy Convers. Manag.* **1999**, *40*, 1713–1721. [\[CrossRef\]](#)
41. Badescu, V. Inference of atmospheric optical depth from near-surface meteorological parameters on Mars. *Renew. Energy* **2001**, *24*, 45–57. [\[CrossRef\]](#)
42. Breus, T.K.; Krymskii, A.M.; Crider, D.H.; Ness, N.F.; Hinson, D.; Barashyan, K.K. Effect of the solar radiation in the topside atmosphere/ionosphere of Mars: Mars Global Surveyor observations. *J. Geophys. Res. Space Phys.* **2004**, *109*, 1–8. [\[CrossRef\]](#)
43. Delgado-Bonal, A.; Martín-Torres, F.J.; Vázquez-Martín, S.; Zorzano, M.-P. Solar and wind exergy potentials for Mars. *Energy* **2016**, *102*, 550–558. [\[CrossRef\]](#)
44. Hourdin, F. A new representation of the absorption by the CO₂ 15- μ m band for a Martian general circulation model. *J. Geophys. Res.* **1992**, *97*, 18319. [\[CrossRef\]](#)
45. Keating, A.; Mohammadzadeh, A.; Nieminen, P.; Maia, D.; Coutinho, S.; Evans, H.; Pimenta, M.; Huot, J.P.; Daly, E. A model for Mars radiation environment characterization. *IEEE Trans. Nucl. Sci.* **2005**, *52*, 2287–2293. [\[CrossRef\]](#)
46. Lee, C.O.; Jakosky, B.M.; Luhmann, J.G.; Brain, D.A.; Mays, M.L.; Hassler, D.M.; Holmström, M.; Larson, D.E.; Mitchell, D.L.; Mazelle, C.; et al. Observations and Impacts of the 10 September 2017 Solar Events at Mars: An Overview and Synthesis of the Initial Results. *Geophys. Res. Lett.* **2018**, *45*, 8871–8885. [\[CrossRef\]](#)
47. Nagaraja, K.; Basuvaraj, P.K.; Chakravarty, S.C.; Kuttanpillai, P.K. Effect of Incoming Solar Particle Radiations on the Exosphere of Mars. *arXiv* **2020**, arXiv:2008.10029.
48. Kamsali, N.; Basuvaraj, P.K.; Chakravarty, S. Effect of Solar Radiation on Exosphere of Mars. *arXiv* **2020**, arXiv:2008.10029. [\[CrossRef\]](#)
49. Nakamura, T.; Tajika, E. Stability of the Martian climate system under the seasonal change condition of solar radiation. *J. Geophys. Res. E Planets* **2002**, *107*, 1–10. [\[CrossRef\]](#)
50. Peterson, W.K.; Thiemann, E.M.B.; Eparvier, F.G.; Andersson, L.; Fowler, C.M.; Larson, D.; Mitchell, D.; Mazelle, C.; Fontenla, J.; Evans, J.S.; et al. Photoelectrons and solar ionizing radiation at Mars: Predictions versus MAVEN observations. *J. Geophys. Res. Space Phys.* **2016**, *121*, 8859–8870. [\[CrossRef\]](#)
51. Pollack, J.B.; Haberle, R.M.; Murphy, J.R.; Schaeffer, J.; Lee, H. Simulations of the general circulation of the Martian atmosphere. 2. Seasonal pressure variations. *J. Geophys. Res.* **1993**, *98*, 3149–3181. [\[CrossRef\]](#)
52. Townsend, L.W.; Pourarsalan, M.; Hall, M.I.; Anderson, J.A.; Bhatt, S.; Delauder, N.; Adamczyk, A.M. Estimates of Carrington-class solar particle event radiation exposures on Mars. *Acta Astronaut.* **2011**, *69*, 397–405. [\[CrossRef\]](#)
53. Wolff, M.J.; Smith, M.D.; Clancy, R.T.; Arvidson, R.; Kahre, M.; Seelos Iv, F.; Murchie, S.; Savijärvi, H. Wavelength dependence of dust aerosol single scattering albedo as observed by the Compact Reconnaissance Imaging Spectrometer. *J. Geophys. Res. E Planets* **2009**, *114*, 12–13. [\[CrossRef\]](#)

54. Zou, H.; Wang, J.S.; Nielsen, E. Reevaluating the relationship between the Martian ionospheric peak density and the solar radiation. *J. Geophys. Res.* **2006**, *111*, A07305. [[CrossRef](#)]
55. Allison, M.; McEwen, M. A post-Pathfinder evaluation of areocentric solar coordinates with improved timing recipes for Mars seasonal/diurnal climate studies. *Planet. Space Sci.* **2000**, *48*, 215–235. [[CrossRef](#)]
56. Madeleine, J.B.; Forget, F.; Head, J.W.; Levrard, B.; Montmessin, F.; Millour, E. Amazonian northern mid-latitude glaciation on Mars: A proposed climate scenario. *Icarus* **2009**, *203*, 390–405. [[CrossRef](#)]
57. Qiu, X.; Zeng, Y.; Liu, C.; Wu, X. Simulation of astronomical solar radiation over Yellow River Basin based on DEM. *J. Geogr. Sci.* **2004**, *14*, 63–69. [[CrossRef](#)]
58. Bennie, J.; Huntley, B.; Wiltshire, A.; Hill, M.O.; Baxter, R. Slope, aspect and climate: Spatially explicit and implicit models of topographic microclimate in chalk grassland. *Ecol. Model.* **2008**, *216*, 47–59. [[CrossRef](#)]
59. Park, J.-K.; Das, A.; Park, J.-H. A new approach to estimate the spatial distribution of solar radiation using topographic factor and sunshine duration in South Korea. *Energy Convers. Manag.* **2015**, *101*, 30–39. [[CrossRef](#)]
60. Piedallu, C.; Gégout, J.-C. Multiscale computation of solar radiation for predictive vegetation modelling. *Ann. For. Sci.* **2007**, *64*, 899–909. [[CrossRef](#)]
61. Sypka, P.; Starzak, R.; Owsiak, K. Methodology to estimate variations in solar radiation reaching densely forested slopes in mountainous terrain. *Int. J. Biometeorol.* **2016**, *60*, 1983–1994. [[CrossRef](#)]
62. Zhang, H.; Liu, G.; Huang, C. Modeling all-sky global solar radiation using MODIS atmospheric products: A case study in Qinghai-Tibet Plateau. *Chin. Geogr. Sci.* **2010**, *20*, 513–521. [[CrossRef](#)]
63. Allen, R.G.; Trezza, R.; Tasumi, M. Analytical integrated functions for daily solar radiation on slopes. *Agric. For. Meteorol.* **2006**, *139*, 55–73. [[CrossRef](#)]
64. Ambreen, R.; Qiu, X.; Ahmad, I. Distributed modeling of extraterrestrial solar radiation over the rugged terrains of Pakistan. *J. Mt. Sci.* **2011**, *8*, 427–436. [[CrossRef](#)]
65. Nettesheim, F.C.; Conto, T.d.; Pereira, M.G.; Machado, D.L. Contribution of Topography and Incident Solar Radiation to Variation of Soil and Plant Litter at an Area with Heterogeneous Terrain. *Rev. Bras. Ciência* **2015**, *39*, 750–762. [[CrossRef](#)]
66. Manara, V.; Beltrano, M.C.; Brunetti, M.; Maugeri, M.; Sanchez-Lorenzo, A.; Simolo, C.; Sorrenti, S. Sunshine duration variability and trends in Italy from homogenized instrumental time series (1936–2013). *J. Geophys. Res.* **2015**, *120*, 3622–3641. [[CrossRef](#)]
67. Manara, V.; Brunetti, M.; Maugeri, M.; Sanchez-Lorenzo, A.; Wild, M. Sunshine duration and global radiation trends in Italy (1959–2013): To what extent do they agree? *J. Geophys. Res.* **2017**, *122*, 4312–4331. [[CrossRef](#)]
68. Tsekouras, G.; Koutsoyiannis, D. Stochastic analysis and simulation of hydrometeorological processes associated with wind and solar energy. *Renew. Energy* **2014**, *63*, 624–633. [[CrossRef](#)]
69. Hemelrijck, E. The effect of orbital element variations on the mean seasonal daily insolation on Mars. *Moon Planets* **1983**, *28*, 125–136. [[CrossRef](#)]
70. Kolb, C.; Abart, R.; Bérces, A.; Garry, J.R.C.; Hansen, A.A.; Hohenau, W.; Kargl, G.; Lammer, H.; Patel, M.R.; Rettberg, P.; et al. An ultraviolet simulator for the incident Martian surface radiation and its applications. *Int. J. Astrobiol.* **2005**, *4*, 241–249. [[CrossRef](#)]
71. Ogibalov, V.P.; Shved, G.M. An improved model of radiative transfer for the NLTE problem in the NIR bands of CO₂ and CO molecules in the daytime atmosphere of Mars. 1. Input data and calculation method. *Sol. Syst. Res.* **2016**, *50*, 316–328. [[CrossRef](#)]
72. Ono, E.; Cuello, J.L. Photosynthetically active radiation (PAR) on Mars for advanced life support. *SAE Tech. Pap.* **2000**, 1–8. [[CrossRef](#)]
73. Cord, A.; Baratoux, D.; Mangold, N.; Martin, P.; Pinet, P.; Greeley, R.; Costard, F.; Masson, P.; Foing, B.; Neukum, G. Surface roughness and geological mapping at subhectometer scale from the High Resolution Stereo Camera onboard Mars Express. *Icarus* **2007**, *191*, 38–51. [[CrossRef](#)]
74. Kreslavsky, M.A.; Head, J.W. Kilometer-scale roughness of Mars: Results from MOLA data analysis. *J. Geophys. Res. Planets* **2000**, *105*, 26695–26711. [[CrossRef](#)]
75. Guo, T.; Yang, X. *ArcGIS Spatial Analysis Experiment Tutorial*; Science Press: Beijing, China, 2006; Volume 196. (In Chinese)
76. Li, F.; Tang, G.; Wang, C.; Cui, L.; Zhu, R. Slope spectrum variation in a simulated loess watershed. *Front. Earth Sci.* **2016**, *10*, 328–339. [[CrossRef](#)]
77. Li, F.; Tang, G.; Wang, C.; Zhang, T. Quantitative analysis and spatial distribution of slope spectrum: A case study in the Loess Plateau in north Shaanxi province. *Geospat. Inf. Sci.* **2007**, *6753*, 67531R. [[CrossRef](#)]
78. Tang, G.; Song, X.; Li, F.; Zhang, Y.; Xiong, L. Slope spectrum critical area and its spatial variation in the Loess Plateau of China. *J. Geogr. Sci.* **2015**, *25*, 1452–1466. [[CrossRef](#)]
79. Tang, G.A.; Li, F.Y.; Liu, X.J.; Long, Y.; Yang, X. Research on the slope spectrum of the Loess Plateau. *Sci. China Ser. E Technol. Sci.* **2008**, *51*, 175–185. [[CrossRef](#)]
80. Wang, C.; Tang, G.; Li, F.; Yang, X.; Ge, S.-S. Fundamental conditions of slope spectrum abstraction and application. *Sci. Geogr. Sin.* **2007**, *27*, 587.
81. Orosei, R. Self-affine behavior of Martian topography at kilometer scale from Mars Orbiter Laser Altimeter data. *J. Geophys. Res.* **2003**, *108*, 8023. [[CrossRef](#)]
82. Rodrigue, C. *Geography of Mars. California Map Society Conference, Long Beach, CA, November*; Science Press: Beijing, China, 2014. Available online: <https://web.csulb.edu/~{rodrigue/mars/cms14/> (accessed on 27 January 2021).

83. Sheehan, W. *Camille Flammarion's the Planet Mars*; Springer: New York, NA, USA, 2015; pp. 435–441. [[CrossRef](#)]
84. Bourke, M.C.; Balme, M.; Beyer, R.A.; Williams, K.K.; Zimbelman, J. A comparison of methods used to estimate the height of sand dunes on Mars. *Geomorphology* **2006**, *81*, 440–452. [[CrossRef](#)]
85. Caldarelli, G.; De Los Rios, P.; Montuori, M.; Servedio, V.D.P. Statistical features of drainage basins in mars channel networks. *Eur. Phys. J. B Condens. Matter Complex. Syst.* **2004**, *38*, 387–391. [[CrossRef](#)]
86. Chapman, M.G.; Allen, C.C.; Gudmundsson, M.T.; Gulick, V.C.; Jakobsson, S.P.; Lucchitta, B.K.; Skilling, I.P.; Waite, R.B. *Volcanism and Ice Interactions on Earth and Mars*; Springer: Boston, MA, USA, 2000; pp. 39–73. [[CrossRef](#)]
87. Hare, T.M.; Skinner, J., Jr.; Liszewski, E.; Tanaka, K.; Barlow, N.G. Mars Crater Density Tools: Project Report. In Proceedings of the 37th Annual Lunar and Planetary Science Conference, League City, TX, USA, 13–17 March 2006; p. 2398.
88. Li, C.; Dong, Z.; Lü, P.; Zhao, J.; Fu, S.; Feng, M.; Zhu, C. A morphological insight into the Martian dune geomorphology. *Chin. Sci. Bull.* **2019**, *65*, 80–90. [[CrossRef](#)]
89. Li, J.; Cao, W.; Tian, X. Topographic surface roughness analysis based on image processing of terrestrial planet. *Clust. Comput.* **2019**, *22*, 8689–8702. [[CrossRef](#)]
90. Badescu, V. *Mars: Prospective Energy and Material Resources*; Springer Science & Business Media: Berlin/Heidelberg, Germany, 2009.
91. O'Gallagher, J.J.; Simpson, J.A. Search for trapped electrons and a magnetic moment at Mars by Mariner IV. *Science* **1965**, *149*, 1233–1239. [[CrossRef](#)]
92. Ward, W.R. Present obliquity oscillations of Mars: Fourth-order accuracy in orbital e and I . *J. Geophys. Res. Solid Earth* **1979**, *84*, 237–241. [[CrossRef](#)]
93. Laskar, J.; Correia, A.C.M.; Gastineau, M.; Joutel, F.; Levrard, B.; Robutel, P. Long term evolution and chaotic diffusion of the insolation quantities of Mars. *Icarus* **2004**, *170*, 343–364. [[CrossRef](#)]
94. Li, X.; Cheng, G.; Chen, X.; Lu, L. Modification of solar radiation model over rugged terrain. *Chin. Sci. Bull.* **1999**, *44*, 1345–1349. [[CrossRef](#)]
95. Zhang, J.; Zhao, L.; Deng, S.; Xu, W.; Zhang, Y. A critical review of the models used to estimate solar radiation. *Renew. Sustain. Energy Rev.* **2017**, *70*, 314–329. [[CrossRef](#)]
96. Wang, S. Study on astronomical solar radiation over rugged terrain using DEM data. In Proceedings of the 2009 First International Conference on Information Science and Engineering, Nanjing, China, 26–28 December 2009; pp. 2184–2187. [[CrossRef](#)]
97. Romana, A.; Xinfu, Q.; Ahmad, I.; Sultan, S. Impact of landforms on the spatial distribution of extraterrestrial solar radiation in the months of March and September: A geographical approach. *Pak. J. Meteorol.* **2012**, *9*, 1–9.
98. Qiu, X.-F.; Zeng, Y.; He, Y.-J.; Liu, C.-M. Distributed Modeling of Diffuse Solar Radiation over Rugged Terrain of the Yellow River Basin. *Chin. J. Geophys.* **2008**, *51*, 700–708. [[CrossRef](#)]
99. Wang, L.; Qiu, X.; Wang, P.; Wang, X.; Liu, A. Influence of complex topography on global solar radiation in the Yangtze River Basin. *J. Geogr. Sci.* **2014**, *24*, 980–992. [[CrossRef](#)]
100. Wilson, J. Mountain Environments and Geographic Information Systems. *N Z Geogr* **1996**, *52*, 50. [[CrossRef](#)]
101. Alvioli, M.; Marchesini, I.; Melelli, L.; Guth, P. *Geomorphometry 2020 Conference Proceedings*; CNR Edizioni: Perugia, Italy, 2020. Available online: https://www.researchgate.net/publication/343537333_Geomorphometry_2020_conference_proceedings (accessed on 27 January 2021). [[CrossRef](#)]
102. Kalogirou, S. Environmental Characteristics. In *Solar Energy Engineering*; Elsevier: Amsterdam, The Netherlands, 2009; pp. 49–762. [[CrossRef](#)]
103. Schmude, R., Jr. The North Polar Cap of Mars. *Ga. J. Sci.* **2014**, *72*, 1.
104. Lowell, P.; Slipher, E. Position of the axis of Mars. *Astron. Nachr.* **1908**, *178*. [[CrossRef](#)]
105. Harvey, D. The Analemmas of the Planets. *Sky Telescope.* **1982**, *6*, 237.
106. Forget, F.; Montmessin, F.; Bertaux, J.L.; González-Galindo, F.; Lebonnois, S.; Quémerais, E.; Reberac, A.; Dimarellis, E.; López-Valverde, M.A. Density and temperatures of the upper Martian atmosphere measured by stellar occultations with Mars Express SPICAM. *J. Geophys. Res. E Planets* **2009**, *114*, 1–19. [[CrossRef](#)]
107. Goddard, N. Accurate analytic representations of solar time and seasons on Mars with applications to the Pathfinder / Surveyor missions mean sun implies a Mars tropical orbit period $s L s$ —• FractionalPart [1 + FractionalPart [Ls]] 360 (O • s) really Tropical *Y. Geophys. Res. Lett.* **1997**, *24*, 1967–1970.
108. Newman, C.E.; Lewis, S.R.; Read, P.L. The atmospheric circulation and dust activity in different orbital epochs on Mars. *Icarus* **2005**, *174*, 135–160. [[CrossRef](#)]
109. Hong, T.; Lee, M.; Koo, C.; Jeong, K.; Kim, J. Development of a method for estimating the rooftop solar photovoltaic (PV) potential by analyzing the available rooftop area using Hillshade analysis. *Appl. Energy* **2017**, *194*, 320–332. [[CrossRef](#)]
110. Corripio, J.G. Vectorial algebra algorithms for calculating terrain parameters from dems and solar radiation modelling in mountainous terrain. *Int. J. Geogr. Inf. Sci.* **2003**, *17*, 1–23. [[CrossRef](#)]
111. Kumar, L.; Skidmore, A.K.; Knowles, E. Modelling topographic variation in solar radiation in a GIS environment. *Int. J. Geogr. Inf. Sci.* **1997**, *11*, 475–497. [[CrossRef](#)]
112. Najafifar, A.; Hosseinzadeh, J.; Karamshahi, A. The Role of Hillshade, Aspect, and Toposhape in the Woodland Dieback of Arid and Semi-Arid Ecosystems: A Case Study in Zagros Woodlands of Ilam Province, Iran. *J. Landsc. Ecol.* **2019**, *12*. [[CrossRef](#)]
113. Zhang, S.; Li, X.; She, J. Error assessment of grid-based terrain shading algorithms for solar radiation modeling over complex terrain. *Trans. GIS* **2019**, *24*, 230–252. [[CrossRef](#)]

114. Serebryakova, M.; Veronesi, F.; Hurni, L. Sine Wave, Clustering and Watershed Analysis to Implement Adaptive Illumination and Generalisation in Shaded Relief Representations. In Proceedings of the 27th International Cartographic Conference, Rio de Janeiro, Brazil, 23–28 August 2015.
115. Hong, T.; Lee, M.; Koo, C.; Kim, J.; Jeong, K. Estimation of the Available Rooftop Area for Installing the Rooftop Solar Photovoltaic (PV) System by Analyzing the Building Shadow Using Hillshade Analysis. *Energy Procedia* **2016**, *88*, 408–413. [[CrossRef](#)]
116. McDonnell, R.; Lloyd, C.; Burrough, P. *Principles of Geographical Information Systems*; Oxford University Press: Oxford, UK, 2015; pp. 7–17.
117. Pro, A. ArcGIS for Desktop. 2018. Available online: <http://pro.arcgis.com/en/pro-app/toolreference/spatial> (accessed on 1 December 2020).
118. Chang, K.-t.; Tsai, B.-w. The Effect of DEM Resolution on Slope and Aspect Mapping. *Cartogr. Geogr. Inf. Syst.* **2013**, *18*, 69–77. [[CrossRef](#)]
119. Aharonson, O.; Zuber, M.; Rothman, D. Statistics of Mars' topography from the Mars Orbiter Laser Altimeter: Slopes, correlations, and physical models. *J. Geophys. Res. Planets* **2001**, *106*, 23723–23735. [[CrossRef](#)]
120. Beyer, R.A.; Kirk, R.L. Meter-scale slopes of candidate MSL landing sites from point photogrammetry. *Space Sci. Rev.* **2012**, *170*, 775–791. [[CrossRef](#)]
121. Garvin, J.; Frawley, J. *Global Vertical Roughness of Mars from Mars Orbiter Laser Altimeter Pulse-Width Measurements*; Lunar and Planetary Science; 2000. Available online: https://www.researchgate.net/publication/4673801_Global_Vertical_Roughness_of_Mars_from_Mars_Orbiter_Laser_Altimeter_Pulse-Width_Measurements (accessed on 27 January 2021).
122. Kreslavsky, M.A.; Head, J.W. Kilometer-scale slopes on Mars and their correlation with geologic units: Initial results from Mars Orbiter Laser Altimeter (MOLA) data. *J. Geophys. Res. Planets* **1999**, *104*, 21911–21924. [[CrossRef](#)]
123. Neumann, G.A. Mars Orbiter Laser Altimeter pulse width measurements and footprint-scale roughness. *Geophys. Res. Lett.* **2003**, *30*, 1561. [[CrossRef](#)]
124. Rosenburg, M.A.; Aharonson, O.; Head, J.W.; Kreslavsky, M.A.; Mazarico, E.; Neumann, G.A.; Smith, D.E.; Torrence, M.H.; Zuber, M.T. Global surface slopes and roughness of the Moon from the Lunar Orbiter Laser Altimeter. *J. Geophys. Res. E Planets* **2011**, *116*, 1–11. [[CrossRef](#)]
125. Shepard, M.K.; Campbell, B.A.; Bulmer, M.H.; Farr, T.G.; Gaddis, L.R.; Plaut, J.J. The roughness of natural terrain: A planetary and remote sensing perspective. *J. Geophys. Res. Planets* **2001**, *106*, 32777–32795. [[CrossRef](#)]
126. Hobson, R.D. *Surface Roughness in Topography: Quantitative Approach*; 1972; pp. 221–245. Available online: <https://oceanrep.geomar.de/37452/> (accessed on 27 January 2021). [[CrossRef](#)]
127. Day, M.J. Surface roughness as a discriminator of tropical karst styles. *Z. Geomorphol.* **2011**, *32*, 1–8.
128. Jones, M.P.; Yoshida, R.K. Fortran Iv Program to Determine the Proper Sequence of Records in a Datafile. *Educ. Psychol. Meas.* **1975**, *35*, 729–731. [[CrossRef](#)]
129. Olaya, V. Chapter 6 Basic Land-Surface Parameters. *Dev. Soil Sci.* **2009**, *33*, 141–169.
130. Hengl, T.; Reuter, H. Geomorphometry: Concepts, software, applications. *Dev. Soil Sci.* **2009**, *33*, 722.
131. Anderson, F.S.; Haldeman, A.F.C.; Bridges, N.T.; Golombek, M.P.; Parker, T.J.; Neumann, G. Analysis of MOLA data for the Mars Exploration Rover landing sites. *J. Geophys. Res. E Planets* **2003**, *108*. [[CrossRef](#)]
132. Tao, J.Y.; Tang, G.A.; Wang, C.; Yang, X. Evaluation of terrain roughness model based on semantic and profile feature matching. *Geogr. Res.* **2011**, *30*, 1066–1076. (In Chinese)
133. Zhu, M.; Li, F.Y. Influence of slope classification on slope spectrum. *Sci. Surv. Mapp.* **2009**, *34*, 165–167.